Earth, Planets and Space

FRONTIER LETTER

Open Access

New aspects of the upper atmospheric disturbances caused by the explosive eruption of the 2022 Hunga Tonga–Hunga Ha'apai volcano

Atsuki Shinbori[1*], Yuichi Otsuka[1], Takuya Sori[1], Michi Nishioka[2], Perwitasari Septi[2], Takuo Tsuda[3], Nozomu Nishitani[1], Atsushi Kumamoto[4], Fuminori Tsuchiya[5], Shoya Matsuda[6], Yoshiya Kasahara[6], Ayako Matsuoka[7], Satoko Nakamura[1], Yoshizumi Miyoshi[1] and Iku Shinohara[8]

Abstract

The Hunga Tonga–Hunga Ha'apai (HTHH) undersea volcanic eruption that occurred at 04:15 UT on 15 January 2022 is one of the most explosive events in the modern era, and a vertical plume reached approximately 55 km, corresponding to a height of the lower mesosphere. The intense explosion and subsequent plume generated acoustic and atmospheric gravity waves detected by ground-based instruments worldwide. Because a global-scale atmospheric and ionospheric response to the large volcanic eruption has not yet been observed, it provides a unique opportunity to promote interdisciplinary studies of coupling processes in lithosphere–atmosphere–ionosphere with ground-based and satellite observations and modeling. Further, this event allows us to elucidate the propagation and occurrence features of traveling ionospheric disturbances, the generation of equatorial plasma bubbles, the cause of electron density holes around the volcano, and the magnetic conjugacy of magnetic field perturbations. The most notable point among these studies is that the medium-scale travelling traveling ionospheric disturbances (MSTIDs) have magnetic conjugacy even in the daytime ionosphere and are generated by an external electric field, such as an E-region dynamo field, due to the motions of neutrals in the thermosphere. This advocates a new generation mechanism of MSTIDs other than the neutral oscillation associated with atmospheric gravity waves and electrified MSTIDs, which are frequently observed during daytime and nighttime, respectively. This paper reviews the recent studies of atmospheric and ionospheric disturbances after the HTHH volcanic eruption and summarizes what we know from this extreme event analysis. Further, we analyzed new datasets not shown in previous studies to give some new insights to understanding of some related phenomena. As a result, we also found that 4-min plasma flow oscillations caused by the acoustic resonance appeared with the amplitude of approximately 30 m/s in the northern hemisphere a few hours before the initial arrival of the air pressure waves. The propagation direction was westward, which is the same as that of the daytime MSTIDs with a magnetic conjugate feature. This result suggests that the 4-min oscillations are generated by an external electric field transmitted to the northern hemisphere along magnetic field lines.

Keywords The Hunga Tonga–Hunga Ha'apai undersea volcanic eruption, Coupling processes in lithosphere–atmosphere–ionosphere, Traveling ionospheric disturbances, Equatorial plasma bubbles, Electron density hole around the volcano, Magnetic conjugacy, E-region dynamo field, Acoustic waves, Atmospheric gravity waves

*Correspondence:
Atsuki Shinbori
shinbori@isee.nagoya-u.ac.jp
Full list of author information is available at the end of the article

Graphical Abstract

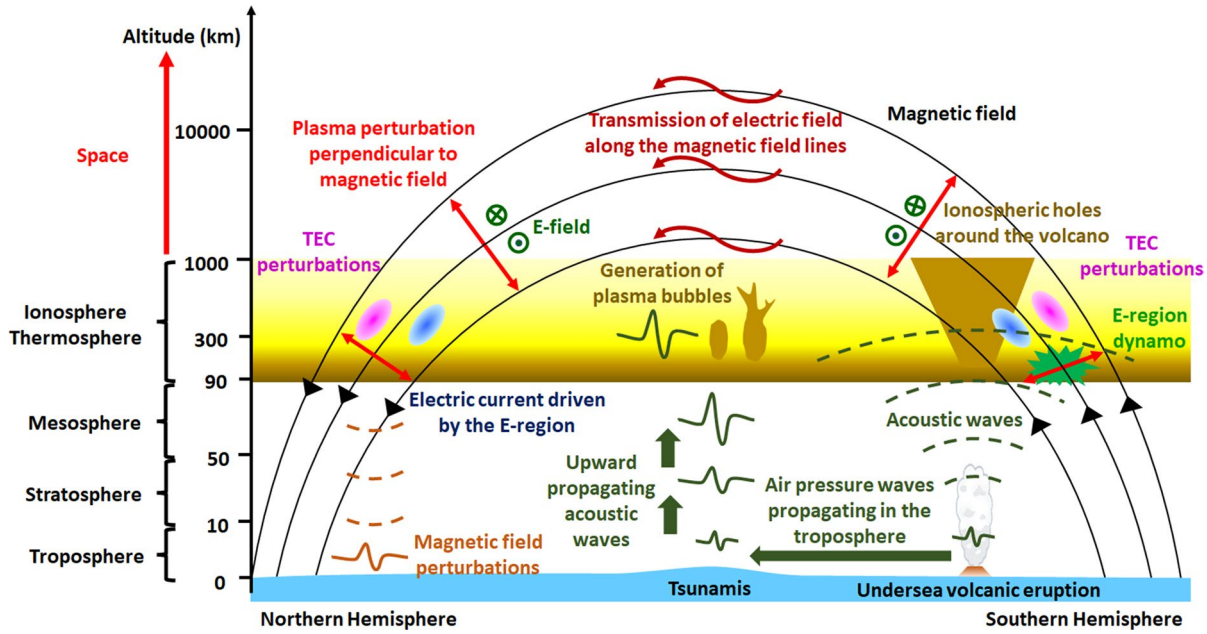

Introduction

Natural hazards caused by severe phenomena of geophysical, hydrological, and meteorological origins negatively impact human activity or the environment. Many people all over the world are threatened by natural hazards every year. Although some natural hazards (typhoons, tornadoes, and floods) can be predicted in near real-time, most geophysical natural hazards, such as earthquakes, volcanic eruptions, and tsunamis, are challenging to forecast. Therefore, we need to rapidly and timely detect the signals of natural geophysical hazards to reduce human loss. Among these geophysical hazards, we experienced the Hunga Tonga–Hunga Ha'apai (HTHH) undersea volcano's explosive eruption at 04:15 UT on 15 January 2022. This eruption is one of the most explosive events in the modern era and generated global atmospheric and ionospheric disturbances in a broad atmospheric region from the troposphere to the ionosphere (Wright et al. 2022) in addition to a tsunami in the Pacific Ocean associated with an air pressure wave (Kubota et al. 2022). The HTHH volcanic eruption provides a unique opportunity to promote interdisciplinary studies of coupling processes in lithosphere–atmosphere–ionosphere to reduce disaster risks.

Astafyeva (2019) has reviewed the detection of ionospheric signals associated with earthquakes, tsunamis, and volcanic eruptions and discussed future perspectives for applications of ionospheric observations to detect natural hazards. This paper reviews the studies of atmospheric and ionospheric disturbances observed after the HTHH volcanic eruption, shows some new insights to the understandings of the phenomena by adding new datasets, and summarizes what we know from existing analyses of this severe event. In this section, we describe several basic concepts of the ionosphere and atmospheric waves for understanding atmospheric and ionospheric disturbances caused by the HTHH volcanic eruption.

Basic features of the Earth's ionosphere

The ionosphere is formed by partial ionization of the upper atmosphere above 60 km altitude due to solar extreme ultraviolet (EUV) radiation and energetic particle precipitation from interplanetary space and the magnetosphere. Percentage of charged particles to neutral atmospheric molecules/atoms increases with altitude. Nevertheless, because the mass of the ionosphere is 10^{12}–10^{13} times smaller than that of the neutral atmosphere, charged particles in the ionosphere are regarded as a minority component in the upper atmosphere (Astafyeva 2019).

The plasma density distribution in the ionosphere depends strongly on latitude, longitude, altitude, and local time. Based on the height profile of electron density,

the ionosphere is classified into several ionospheric regions: D (60–90 km), E (90–150 km), and F (150–1000 km). The height of the maximum electron density is typically located at an altitude of ~ 250–400 km. Such the electron density profile is determined by the ionization of neutral particles, their recombination processes, dynamics, and electrodynamics in the upper atmosphere and ionosphere. Further, the ionosphere highly varies through solar/geomagnetic activities and upward propagating atmospheric waves originating from lower atmospheric disturbances (Hargreaves 1992; Kelley 2009).

Because the ions in the E region frequently collide with the neutral upper atmosphere, this process causes electric current in the ionosphere and a dynamo electric field through momentum transfer by ion-neutral collisions (e.g., Maeda and Kato 1966; Richmond 1979). The dynamo electric field is transmitted along magnetic field lines to the F region of the ionosphere and causes the plasma density perturbations driven by $\mathbf{E} \times \mathbf{B}$ drift of ionospheric plasma (e.g., Yamazaki and Maute 2017; Shinbori et al. 2022). The spatial inhomogeneity of ionospheric conductivity due to the plasma density perturbations creates a polarization electric field to keep the current continuity. Oscillations of the neutral atmosphere or polarization electric fields can generate traveling ionospheric disturbances (TIDs). Some of the TIDs can subsequently initiate equatorial plasma bubbles (EPBs).

Basic properties of atmospheric acoustic and gravity waves

Transient perturbations near the Earth's surface associated with earthquakes, Rayleigh waves, volcanic eruption, nuclear explosions, rocket launches, tsunamis, and severe tropospheric events (tropical storms, typhoons, and hurricanes) become a seed of acoustic and gravity waves propagating to the upper atmosphere (e.g., Afraimovich et al. 2001; Afraimovich et al. 2013; Artru et al. 2004; Blanc 1985; Calais et al. 1998; Calais and Minster 1998; Chou et al. 2017; Dautermann et al. 2009a, b; Fritts and Alexander 2003; Heki and Ping 2005; Hines 1960; Nishioka et al. 2013; Occhipinti et al. 2013; Pokhotelov et al. 1995; Rolland et al. 2010). Because the atmospheric density exponentially decreases with increasing altitude, the amplitude of both acoustic and gravity waves grows as they propagate upward according to the energy conservation law (Hines 1960). However, a reduction in the wave amplitude also occurs due to the dissipation of the wave energy associated with molecular viscosity and thermal conductivity in the thermosphere (Hines 1960). Therefore, the damping rate becomes more significant with a decreased atmospheric density. Thus, the amplitude reaches the maximum value at an altitude of ~ 200–300 km for waves with a period of several tens of minutes (Blanc et al. 2010).

The acoustic waves exist above the acoustic cutoff frequency ($\omega_a \geq 3.3$ mHz) and lead to pressure change due to compression and rarefaction of the atmosphere (Hargreaves 1992). The wave propagation speed equals the sound speed of ~ 330 m/s on the ground and increases to 800 m/s in the thermosphere at a 250–300 km altitude. Therefore, it takes 8–9 min for the acoustic waves to reach the ionosphere. On the other hand, gravity waves with longer wavelengths displace parcels of atmospheric mass according to the balance between the force of gravity and buoyancy (Fritts and Alexander 2003; Hargreaves 1992). The gravity waves exist below the Brunt-Väisälä frequency ($\omega_{ag} \leq \omega_b \cong 2.9$ mHz in the troposphere). They cannot propagate vertically but in the oblique direction with a much slower sound speed. The direction of the group velocity is perpendicular to that of the phase velocity in the vertical direction (Hines 1960; Huang et al. 2019). Because of the slow speed, the travel time of gravity waves with a period of 10–15 min and horizontal phase velocity of 200–310 m/s from the ground to the ionosphere is estimated as 45–60 min (Astafyeva 2019).

When the atmospheric acoustic and gravity waves reach the ionosphere, the ionospheric plasma density fluctuates through dynamical and photochemical processes associated with the neutral atmospheric oscillations of these waves. In the region above 250 km, the atmospheric waves dominantly interact with ionospheric plasmas through momentum transfer by collisions of neutral particles with ions. Because the charged particles can move along the magnetic field line at the same velocity as ions, the velocity V_i can be written as $V_i = V_n \cos\theta$, where V_n is the neutral particle velocity and θ is the angle between the magnetic field line and direction of the neutral particle oscillation. Figure 1 summarizes schematically the characteristics of upward propagating atmospheric acoustic and gravity waves associated with a volcanic eruption.

An overview of the HTHH volcanic eruption and related phenomena

The HTHH volcano is located at 20.536° S, 175.382° W in the southwest Pacific Ocean and is one of the undersea volcanos rising from the seafloor to the sea surface. Remnant of the northern and western outer edges of the volcanic caldera form two islands each with a length of 2 km. The northern and western islands are named Hunga Tonga and Hunga Ha'apai. The HTHH volcano has been active since an underwater explosion south of Hunga Tonga occurred in 1912. All recorded eruptions were along the rim of the underwater caldera (Fig. 2). During an explosive eruption from December 2014 to

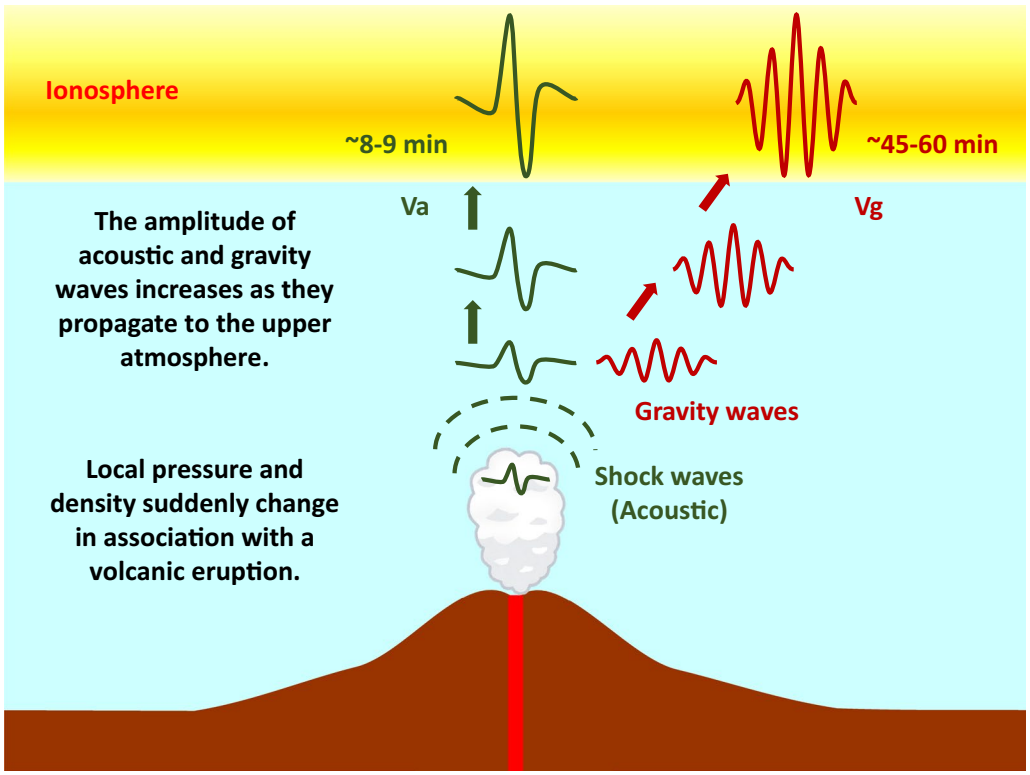

Fig. 1 Schematic view of generation of atmospheric and ionospheric disturbances associated with a volcanic eruption. After the onset of a volcanic eruption, acoustic and gravity waves are generated by local pressure and density variations. The amplitude grows with increasing altitude. The acoustic waves propagating at the sound velocity (Va) arrive in the ionosphere within ~ 8–9 min after the onset of a volcanic eruption. Because the propagation velocity of the gravity waves is much slower than that of the acoustic waves, the gravity waves reach the ionosphere within ~ 45–60 min after the eruption

January 2015, a tuff cone appeared over the sea level, connecting the Hunga Ha'apai and Hunga Tonga islands (Garvin et al. 2018). The new island existed over the sea surface until a large eruption destroyed it, leaving only the two small islands. On 15 January 2022, the HTHH volcano erupted with two main explosions that released an enormous amount of energy into the atmosphere. Different types of atmospheric and ionospheric disturbances after the eruption were globally observed with other techniques. Due to the extensive feature, many researchers in various fields have studied this event.

The unique and explosive eruption of the HTHH volcano eruption on 15 January 2022 provided us with a few important aspects: the exact onset time of the eruption, the energy release into the lithosphere and atmosphere, the time evolution of the ash plume, global atmospheric oscillations, and the tsunami caused by this eruption. According to the United States Geological Survey (USGS) earthquake catalog, this event has been recorded as an earthquake with magnitude scale 5.8 that occurred at 04:14:45 UT. The equivalent energy released in the lithosphere was inferred between 4 and 18 Megaton of trinitrotoluene (TNT) (Garvin et al. 2022), while that in the atmosphere and ionosphere was estimated as 50 Megaton (Campbell-Brown et al. 2022), more than 58 Megaton (Kulichkov et al. 2022) and 9–37 Megaton (Astafyeva et al. 2022). The volcanic explosivity index (VEI) value is estimated at 5 (Zhao et al. 2022). The ash plume reached ~ 55 km in the mesosphere and 600 km in diameter, captured by satellite images (National Aeronautics and Space Administration (NASA) 2022). This eruption generated atmospheric waves (e.g., Lamb waves, acoustic waves, and gravity waves), ionospheric disturbances, geomagnetic field variations, tsunamis, and seismic waves observed all over the world (e.g., Aa et al. 2022a; Aryal et al. 2023; Astafyeva et al. 2022; Boyde et al. 2022; Carr et al. 2022; Carter et al. 2023; Chen et al. 2022, 2023; Chum et al. 2023; Dorrian et al. 2023; Gavrilov et al. 2022; Ghent and Crowell 2022; Han et al. 2023; He et al. 2023; Heki 2022; Hong et al. 2022; Iyemori et al. 2022; Kong et al. 2023; Kubota et al. 2022; Kundu et al. 2023; Le et al. 2022; Li et al. 2023a, b; Lin et al. 2022; Liu et al. 2023; Madonia et al. 2023; Maletckii and Astafyeva 2022; Matoza et al. 2022; Muafiry et al. 2022; Omira

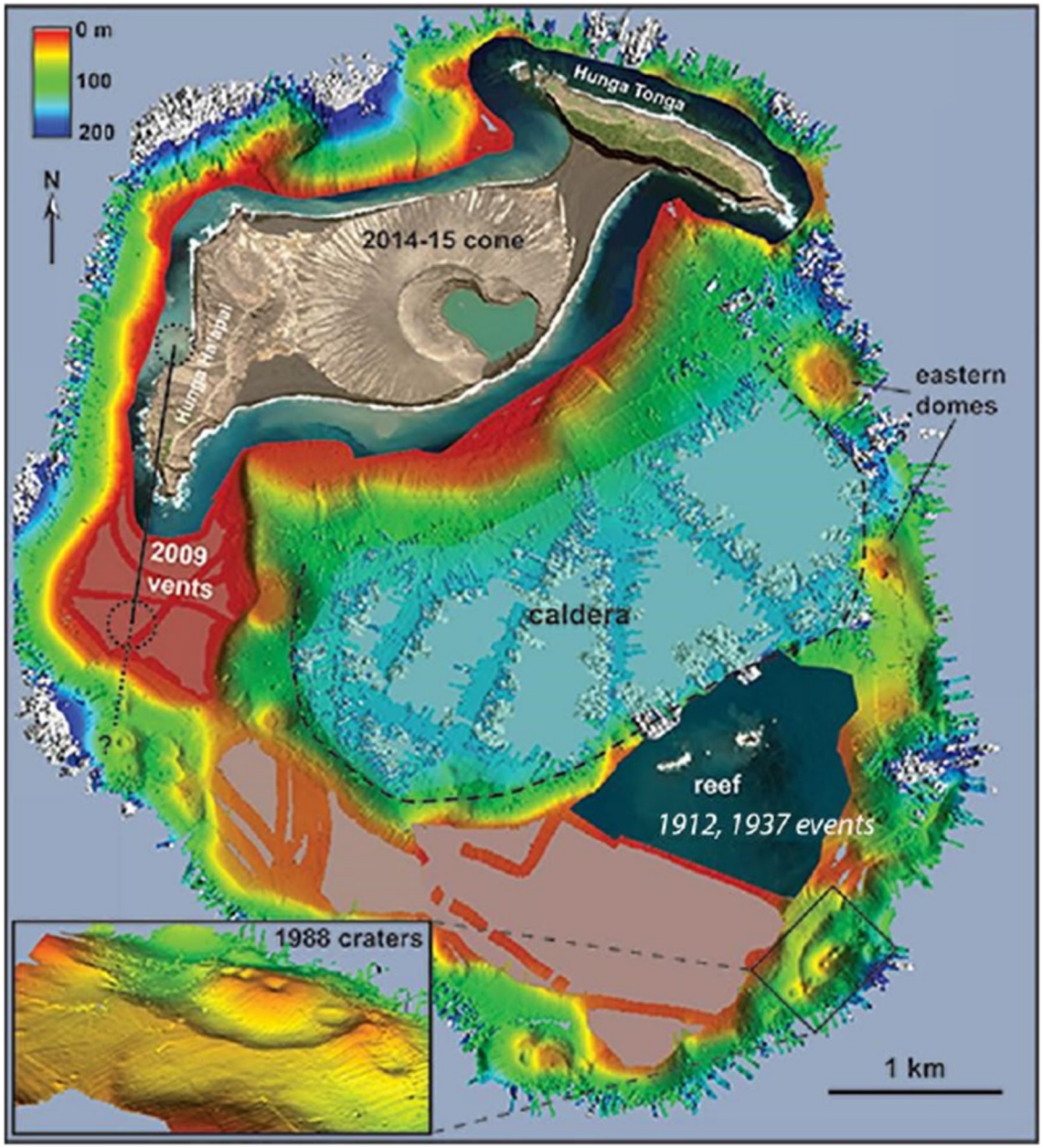

Fig. 2 Two-dimensional map of the summit platform of the submerged HTHH volcanic edifice. The color bar of the upper left side shows the depth of the sea surface in a unit of meters. The dashed black line indicates a previously undocumented caldera existing 150 to 180 m below the sea surface. The close-up view of the bottom left side represents the detailed locations of the 1988 eruptions (Cronin et al. 2017)

et al. 2022; Pradipta et al. 2023; Rajesh et al. 2022; Rakesh et al. 2022; Ravanelli et al. 2023; Saito 2022; Schnepf et al. 2022; Shinbori et al. 2022; Sun et al. 2022a, b; Tang 2023; Takahashi et al. 2023; Tanioka et al. 2022; Themens et al. 2022; Vadas et al. 2023a, b; Verhulst et al. 2022; Watanabe et al. 2022; Yamazaki et al. 2022; Wang et al. 2022; Zhou et al. 2022). The dynamo electric field generated by thermospheric natural wind disturbances due to the HTHH volcanic eruption modified the plasma density structure of equatorial ionization anomaly in the American longitude (e.g., Aa et al. 2022b; Zhang et al. 2022a, b). Lightning activities were also enhanced significantly after the HTHH volcanic eruption (e.g., Bor et al. 2023; Mezentsev et al. 2023; Nickolaenko et al. 2022). In the following section, we will mainly survey the characteristics of upper atmospheric disturbances (ionospheric and magnetic

field perturbations) detected by various kinds of ground-based instruments and satellites after the 15 January 2022 HTHH volcanic eruption and discuss their generation mechanism from the viewpoint of coupling processes in the lithosphere–atmosphere–ionosphere.

Effects of the explosive eruption of the HTHH volcano on the upper atmosphere

Global propagation features of traveling ionospheric disturbances

As described in "Basic properties of atmospheric acoustic and gravity waves" section, the sudden displacement of the earth's surface associated with earthquakes, tsunamis, and volcanic eruptions generates atmospheric waves that propagated to the upper atmosphere. Neutral oscillations in this region due to the atmospheric waves caused TIDs in the ionosphere. Using total electron content (TEC) and high-frequency Doppler sounding observations, Ogawa et al. (1982) found that TIDs generated after the large eruption of Mount St. Helens in 1980 propagated across the Pacific Ocean to Japan. They estimated the horizontal speed of ionospheric disturbances (with a period of ~ 9 min) as ~ 300 m/s corresponding to the propagation speed of a Lamb wave. They interpreted that the ionospheric disturbances are caused by upward propagating waves coupled with the Lamb wave. Cheng and Huang (1992) also found TIDs after the large eruption of Mount Pinatubo in 1991. Nowadays, ionospheric TEC observation with the global navigation satellite system (GNSS) receiver network enabled us to monitor global ionospheric disturbances with high time and spatial resolution. Many researchers reported ionospheric disturbances associated with large volcanic eruptions in the world using GNSS-TEC observation data (e.g., Astafyeva 2019; Dautermann et al. 2009a, b; Heki 2006; Manta et al. 2021; Meng et al. 2019; Nakashima et al. 2016; Shults et al. 2016; Cahyadi et al. 2021; Shestakov et al. 2021; Heki and Fujimoto 2022). The ionospheric disturbances with periods of 12–30 min usually appear approximately 10–45 min after the onset of the volcanic eruption and can be observed from the volcano to a long distance (> 800 km). The time difference of the onsets between the volcanic eruption and ionospheric disturbances corresponds to the propagation time of atmospheric waves from the surface to the ionosphere. The horizontal propagation speed of the ionospheric disturbances is between 300 and 1100 m/s, equal to that of acoustic gravity waves, acoustic waves, and shock-acoustic waves.

Figure 3 shows the time-series plots of the detrended TEC subtracted from the 30-min running average at several GNSS stations in New Zealand (A), Australia (B), Japan (C), Eastern Canada (D), South Africa (E), and Northern Europe (F). To compare the propagation between the ionospheric perturbations and Lamb waves at the surface, the height variation of the neutral atmosphere calculated with the transient inertia gravity and rossby wave dynamics (TIGAR) model is overplotted in each panel in Fig. 3. In these panels, the TEC perturbations with their amplitude of 0.5–2.0 TECU appear in all regions, almost coinciding with an initial arrival of the Lamb waves at the surface. This is the first result demonstrating the global impact of the HTHH eruption on the ionosphere reported by Themens et al. (2022). Such a global signature of ionospheric disturbances associated with a volcanic eruption had not been reported in the past. Themens et al. (2022) also found two distinct large scale ionospheric traveling ionospheric disturbances (LSTIDs) and several subsequent medium scale traveling ionospheric disturbances (MSTIDs) that propagate outward from the epicenter of the HTHH volcanic eruption. The initial propagation speed of the LSTID with a wavelength of > 1600 km was ~ 950 m/s, which is close to the acoustic speed at the F-region peak. The propagation speed decreased to ~ 700 m/s at a distance of ~ 2300 km from the epicenter. MSTIDs with a speed of 200–400 m/s continued to be generated near the epicenter for 6 h following the event. Astafeva et al. (2022), for the first time, identified five main eruptions based on the N-shaped TEC variations during 04:30–05:30 UT on 15 January 2022. Deducing from previous studies showing that the amplitude of the TEC perturbations is proportional to the VEI value (Shults et al. 2016), Astafeva et al. (2022) estimated that the major eruption at 04:18:10 UT released a huge amount of energy between 9 and 37 Megaton in TNT equivalent. This energy is comparable to the 1883 Krakatoa volcanic eruption. Using quasi-zenith satellite system (QZSS)-TEC observation data in Japan, Heki (2022) showed that ionospheric disturbances propagating as fast as the Lamb wave were triggered by the HTHH volcanic eruption. He also found a rapid increase of TEC that started ~ 40 min before the initial arrival of the Lamb wave from a comparison with several barometer data, as shown in Fig. 4. He interpreted that the ionospheric disturbances are driven by forward energy leakage of the acoustic waves propagating in the ionosphere/thermosphere, which were waster the Lamb waves in the troposphere. Detailed physical mechanisms should be solved in future studies.

Taking advantage of the dense GNSS receiver network in New Zealand, Australia, and Japan, Lin et al. (2022) found that TIDs appeared over Japan approximately 3 h before the initial arrival of an air pressure wave in the troposphere. The waveform of TIDs over Japan is almost consistent with that over Australia (Fig. 5), and the TIDs have a magnetic conjugate feature. Because the TIDs appeared over Australia a few hours before the

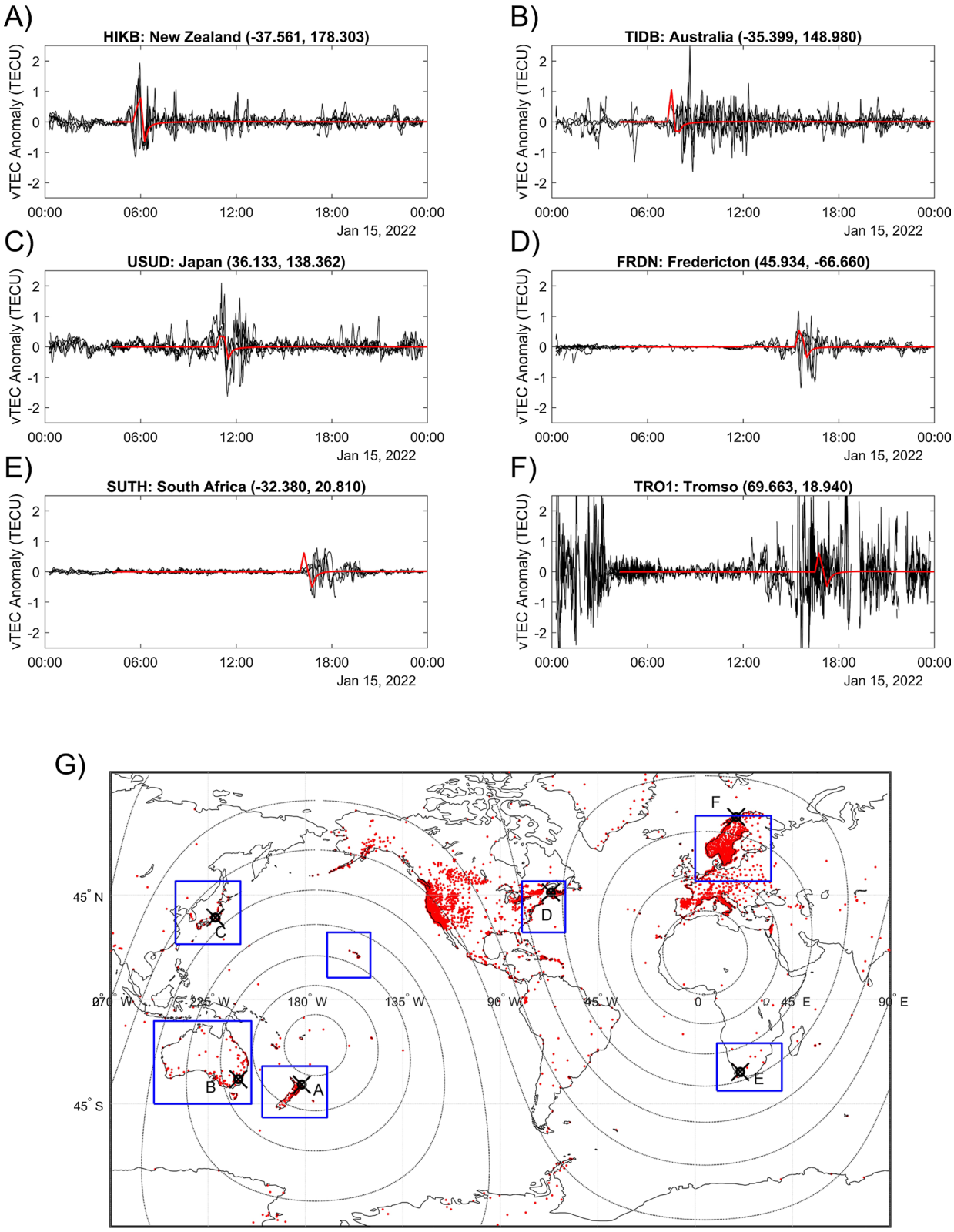

Fig. 3 Time-series plots of detrended TEC (black) and TIGAR-modeled height variation in units of 0.01 m (red) for stations in New Zealand (**a**), Australia (**b**), Japan (**c**), Fredericton (**d**), South Africa (**e**), and Tromso (**f**). Panel **g** Map of GNSS receiver stations (red). The locations of the stations in **a**–**f** are marked with black "x" symbols. A constant distance from the epicenter of the HTHH eruption every 1500 km is presented as dotted circles (Themens et al. 2022)

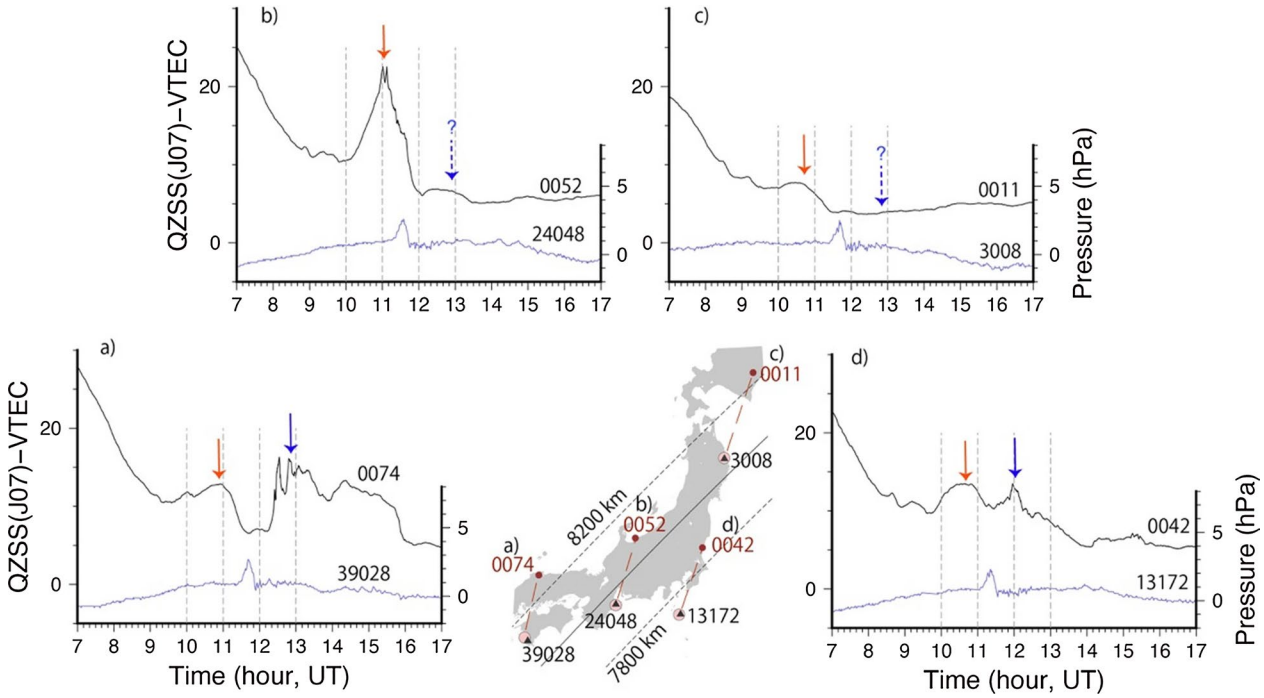

Fig. 4 Comparison of the pressure (blue) and TEC (black) variations obtained by the geostationary satellite J07 on 15 January around the first passage of the Lamb wave. Locations of GNSS stations (red circles), their sub-ionospheric points (pink circles), and barometers near sub-ionospheric points (black triangles) are indicated in a center map with labels **a**–**d**. SIPs and GNSS stations are tied with red dashed lines. Two TEC peaks are indicated by blue and red arrows, but only the first peak is clear in panels **b**, **c** (Heki 2022)

conventional tsunami reached the Australian coasts, Han et al. (2023) discussed the possibility of developing tsunami warning systems by monitoring ionospheric variations with GPS-TEC measurements. Lin et al. (2022) interpreted that the TIDs are driven by electromagnetic coupling through the magnetic field lines in both hemispheres. This finding implies that the atmospheric disturbances triggered by the HTHH volcanic eruption could generate the TIDs with magnetic conjugacy even in the daytime, which had not been previously reported in the literature. To investigate the magnetic conjugate feature of the TIDs, Shinbori et al. (2022) compared the global GNSS-TEC data with the ionospheric plasma flow data obtained from the super dual auroral radar network (SuperDARN) Hokkaido pair of radars (Nishitani et al. 2019). As a result, Shinbori et al. (2022) found the plasma flow perturbations in the F-region corresponding to the TEC perturbations with a magnetic conjugate feature. However, they did not show whether or not an analogous magnetic conjugate feature can be seen in the plasma flow and detrended TEC data when the air pressure wave passed through the field-of-view (FOV) of the SuperDARN radar. For this reason, we investigate the relationship between the northward plasma flow in the northern hemisphere and detrended TEC in the southern hemisphere in addition to the results reported by Shinbori et al. (2022). Figure 6 shows a range-time plots of (a) northward plasma flow, (b) 15-min high-pass filtered northward plasma flow, (c) and (e) temperature deviation in the northern and southern hemispheres, respectively, and (d) detrended TEC in the southern hemisphere. In Fig. 6, the two distinct plasma flow perturbations with an amplitude of ~ 100 m/s were observed around 08:00 and 09:00 UT in the northern hemisphere, simultaneously with the onset of the TEC perturbations after the arrival of air pressure waves in the southern hemisphere (Shinbori et al. 2022). A similar feature of the plasma flow variations in the ionosphere was reported by Zhang et al. (2022a, b). They further pointed out that the plasma flow speed was faster in the E-region than in the F-region. In this case, the southern hemisphere corresponds to a sunlit region where the ionospheric integrated Hall and Pedersen conductivities are 6.8 and 5.5 S, respectively, when we estimated them with an ionospheric conductivity calculation tool (Koyama et al. 2014). On the other hand, the air pressure waves passed through the FOV of the SuperDARN radar during 12:00–13:00 UT shown in Fig. 6g. Associated with the arrival of the air pressure waves, the northward plasma flow was observed with an amplitude of ~ 100 m/s, and then the flow direction was changed from northward to southward. In this case, the TEC perturbations corresponding to the plasma flow

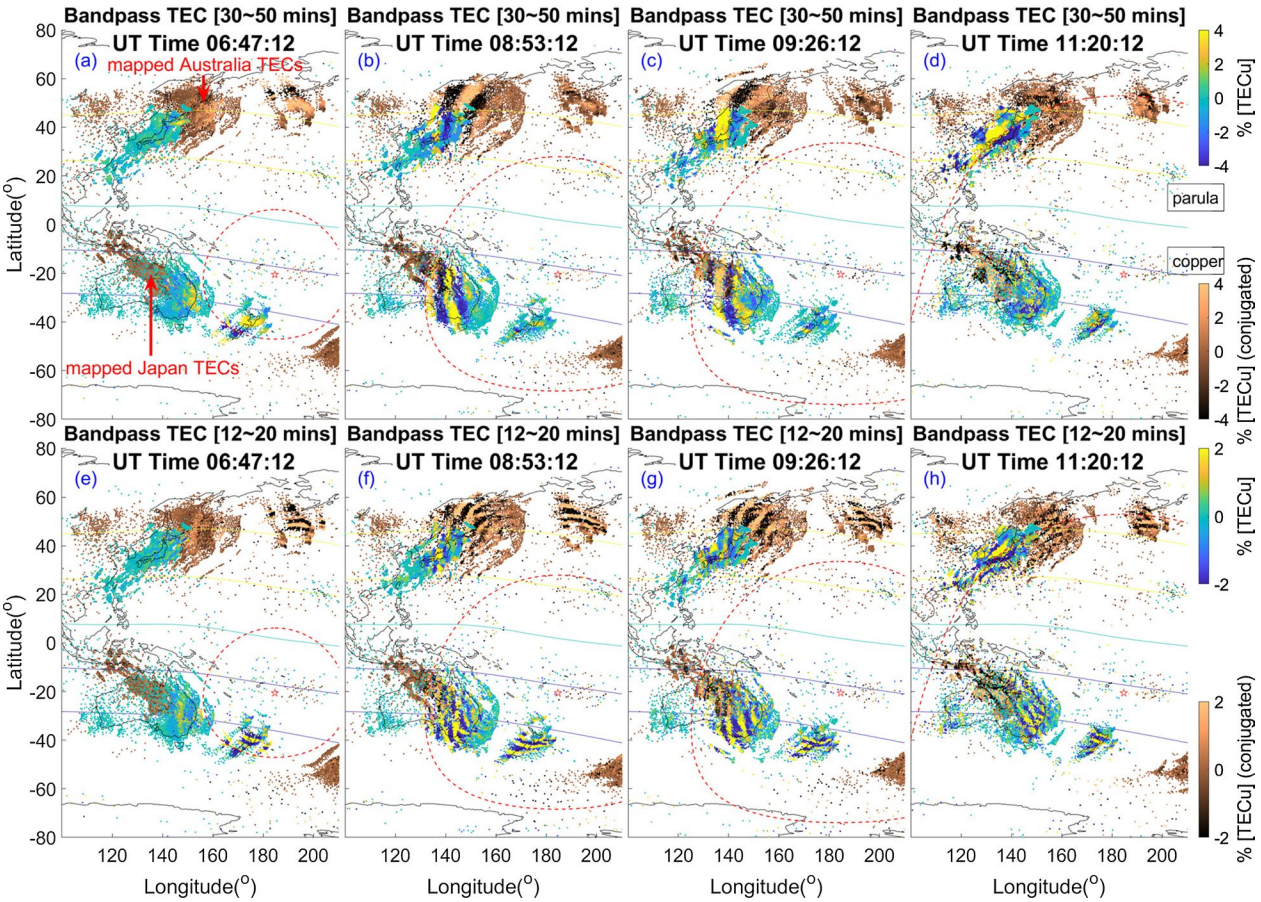

Fig. 5 Two-dimensional maps of band-pass filtered TECs of **a**–**d** 30–50 min and **e**–**h** 12–20 min periods overplotting the conjugate concentric TIDs after mapping Japan (Australia) TECs to Sothern (Northern) hemisphere. The original and conjugate TECs are indicated by the parula and copper color codes, respectively. The red-dashed circle shows the propagation of the Lamb wave at ~315 m/s (Lin et al. 2022)

variations cannot be seen in the southern hemisphere (panel d). At this time, the northern hemisphere is a dark region where the ionospheric integrated Hall and Pedersen conductivities are 0.08 and 0.58 S, respectively. These values are two orders of magnitude smaller than those in the sunlit region. Therefore, the present analysis result suggests that high ionospheric conductivities in the sunlit region are necessary to manifest the magnetic conjugate TIDs. Further, Shinbori et al. (2022) found a significant phase difference of 10–12 min between the TEC and plasma flow perturbations. They reproduced this relationship from a simple ionospheric model calculation with an external electric field as an input parameter. This result suggests that the magnetic conjugate TIDs are generated by an external electric field driven by an E-region dynamo. Jonah et al. (2017), for the first time, found the occurrence of the daytime MSTIDs with a magnetic conjugate feature over the Brazilian sector based on the GPS-TEC analysis. They proposed that the atmospheric gravity wave-induced electric fields from one hemisphere mapped along the magnetic field lines and generate the mirrored MSTIDs in the magnetic conjugate region. The generation mechanism described above differs from normal MSTIDs due to atmospheric gravity waves in the daytime and Perkins instability (Perkins 1973) in the nighttime. Thus, the explosive HTHH volcanic eruption provides an excellent opportunity to study wind-dynamo coupling to drive the magnetic conjugate TIDs in the daytime. Considering the results reported by Jonah et al. (2017), we need to clarify the occurrence feature of the daytime MSTIDs with magnetic conjugacy based on a statistical analysis of global GNSS-TEC data.

Rapid changes of the E-region dynamo and thermospheric wind

As described in "Global propagation features of traveling ionospheric disturbances" section, the HTHH volcanic eruption generated global atmospheric and ionospheric disturbances observed with various kinds of ground-based and satellite instruments. This volcanic

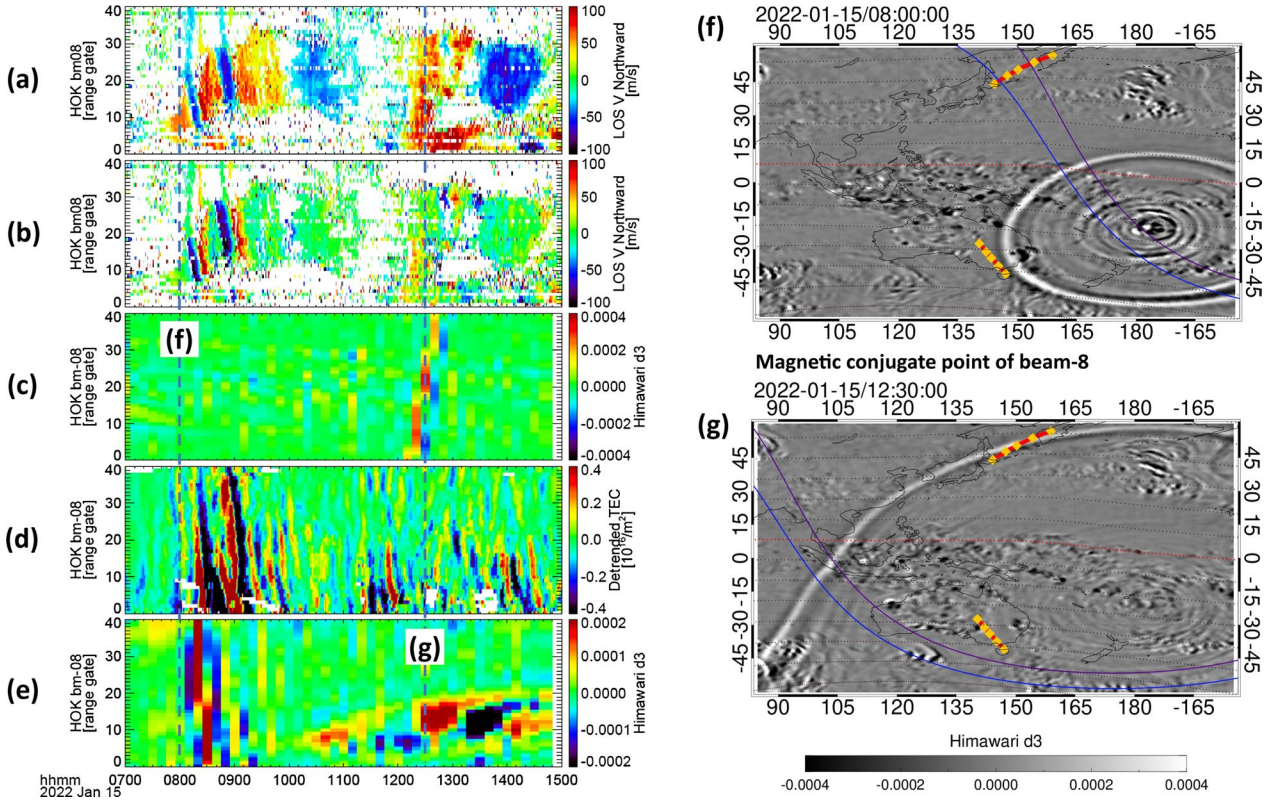

Fig. 6 Range-time plots of **a** northward plasma flow, **b** 15-min high-pass filtered northward plasma flow, **c**, **e** temperature deviation, and **d** detrended TEC. The first three panels show the data along the beam-8 direction of the SuperDARN radar in the northern hemisphere, indicated by the red line in panels **f**, **g**, while the rest panels show the data along the magnetically conjugate beam-8 direction in the southern hemisphere. Panels **f**, **g** show the two-dimensional map of temperature deviation at 08:00 and 12:30 UT on 15 January 2022. These times are represented by the vertical dashed lines in the left panel. The blue and red curves indicate the sunset terminator at an altitude of 105 and 300 km, respectively

eruption also caused a rapid change in the E-region dynamo and thermospheric wind pattern. Using ion density and drift velocity data obtained from the ICON satellite, Gasque et al. (2022) found extreme zonal and vertical electric field ion drifts ~ 4000 km away from the HTHH volcano within 1 h of the eruption before the initial arrival of atmospheric disturbances. The period and amplitude of the vertical ion drift were ~ 6 min and ~ 100 m/s, respectively. The observation point was almost consistent with the magnetically conjugate E-region just 400 km from the HTHH volcano. This result suggests that the electric field generated by the E-region dynamo around the HTHH volcano is transmitted along the magnetic field lines. Gasque et al. (2022) also estimated the amplitude of thermospheric wind perturbations as more than 200 m/s based on the observed ion drift velocity and a simple theoretical model.

After the air pressure wave passed through the dayside, the Swarm A and Ionospheric Connection Explorer (ICON) satellites observed the direction change of the equatorial electrojet (EEJ) and neutral wind (90–300 km) (Fig. 7). In Fig. 7g, h, the height profile of the zonal wind shows an enhancement of eastward and westward winds in the Hall (90–110 km) and Pedersen (120–150 km) regions, respectively, when the EEJ is directed westward (Fig. 7f). This relationship between the EEJ and thermospheric neutral wind is almost consistent with that

(See figure on next page.)

Fig. 7 **a**, **b** Trajectories of the ICON (red) and Swarm (green) satellites, ground magnetic observatories (yellow), and a wavefront of the air pressure wave from the HTHH volcano with the propagation speed of 318 m/s (black). Dots indicate each satellite location at the given time. **c**, **d** Height profiles of zonal wind at the exact locations above (**e**, **f**) EEJ observations on each orbit of the Swarm A satellite. **g**, **h** Height profiles of zonal wind on each orbit of the ICON satellite. The statistical value of the background wind (gray shaded areas and solid black lines) corresponds to percentiles of the entire data set. The background wind (black dotted line) is calculated with the four previous days (Harding et al. 2022)

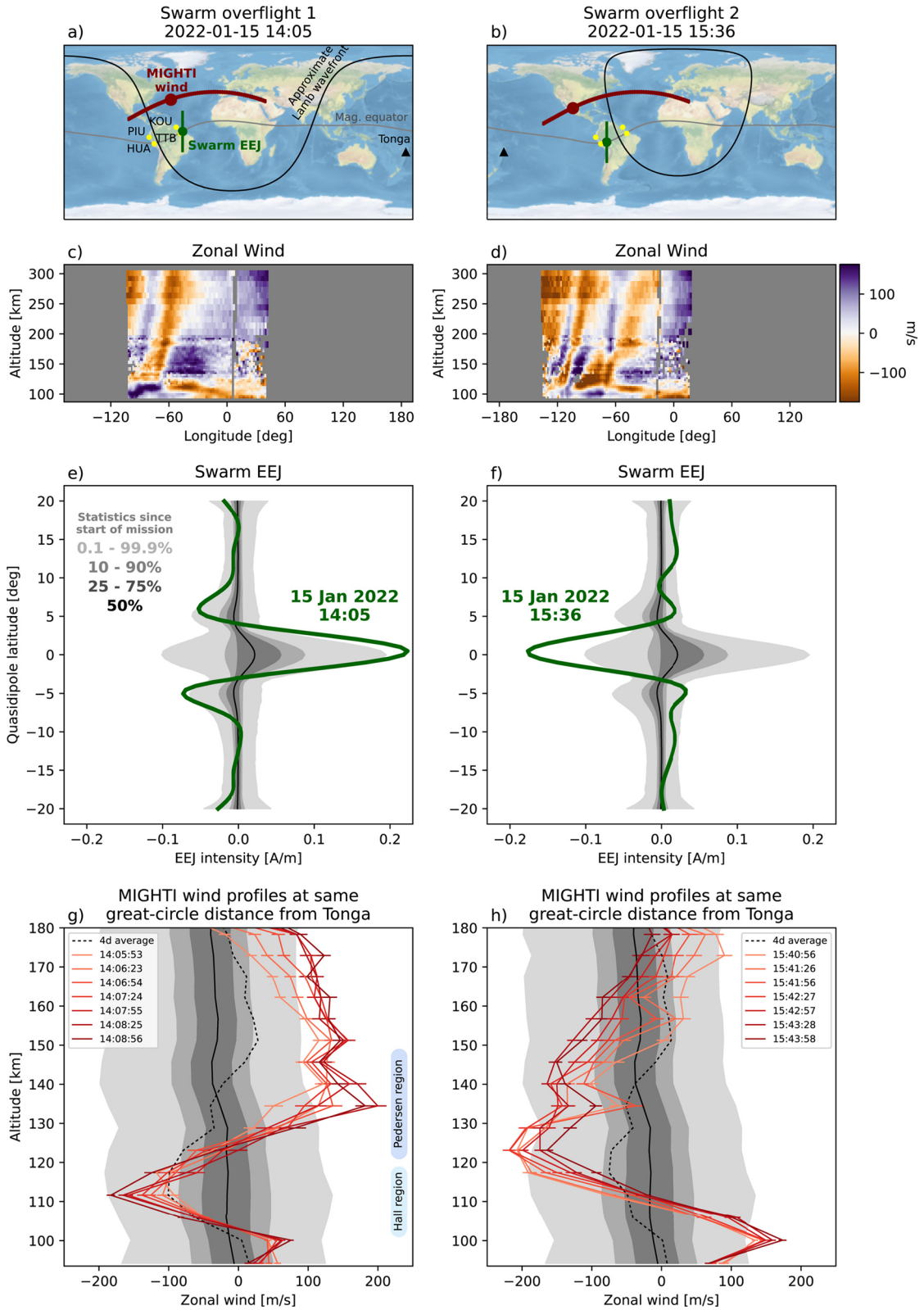

Fig. 7 (See legend on previous page.)

reported by Yamazaki et al. (2014) and Yamazaki et al. (2021). The physical meaning of the anti-correlation between the EEJ and the thermospheric neutral wind is the local generation of the electric field. In the Hall region, an eastward wind generates an upward dynamo electric field which drives the eastward current due to the westward drift of the electrons. Finally, the westward electric field is generated in the Hall region. In the Pedersen region, an eastward wind generates an upward current due to the upward dynamo electric field. This current produces a downward electric field. The electric field is mapped onto the Hall region and drives the westward current off the equatorial region in both hemispheres. Finally, this current generates an eastward electric field. As a result, the westward EEJ is observed near the equatorial region. Le et al. (2022) also showed that strong eastward turning of zonal wind in the E-region leads to the direction change of the EEJ using space- and ground-based observation data. The effect of neutral wind on the EEJ had been predicted by Yamazaki et al. (2014), and a few years later Harding et al. (2022) demonstrated through observations that the neutral wind in the thermosphere plays an important role in the EEJ perturbations based on integrated data analysis of upper atmospheric disturbances after the large HTHH volcanic eruption.

Using the data of the X- and Y-components of the geomagnetic field obtained at 13 geomagnetic observatories from mid-latitudes to the equator, Sun et al. (2022a, b, c) showed that the HTHH volcanic eruption caused perturbations of the E-region current density by 22–55 mA/m within a radius of 8000 km from the HTHH volcano. Corresponding to the appearance of the ionospheric currents, the TEC data showed the start of ionospheric electron density variation in the F-region at an altitude of ~ 350 km. From the onset of the magnetic field perturbations, Sun et al. (2022a, b, c) estimated the propagation speed of the leading front as ~ 740 m/s, which corresponds to the acoustic velocity in the ionosphere (thermosphere) at an altitude of 200–300 km (Shinbori et al. 2023). The magnetic field disturbances from several minutes to hours persisted for more than 10 h after the HTHH eruption.

It is well-known that geomagnetic field variation associated with acoustic waves is frequently observed with a period of several mHz range after earthquakes and volcanic eruptions (e.g., Iyemori et al. 2005; Hasbi et al. 2009; Aoyama et al. 2016; Zettergren and Snively 2019). Also, in the case of the HTHH volcanic eruption, the geomagnetic field oscillations were observed in the pulsations continuous (Pc) 5 range (150–600 s or 1.7–6.7 mHz) (Fig. 8). The dominant frequency of the geomagnetic field oscillations was 3.8 mHz, which is almost equal to the acoustic resonance frequency (e.g., Inchin et al. 2020; Kanamori et al. 1994; Lognonné et al. 1998; Matsumura et al. 2012, 2011; Shinagawa et al. 2007; Tahira 1995). This frequency corresponds to the period required for the acoustic waves to go back and forth between the ground and the ionosphere. Yamazaki et al. (2022) described that the amplitude of the geomagnetic field oscillations reached ~ 3 nT at Apia, located 835 km north-northeast of the HTHH volcano, which is much larger than those during other events previously reported. Further, Yamazaki et al. (2022) found that the waveform of the geomagnetic field oscillations at Apia resembles the waveform observed at Honolulu, located near the magnetic conjugate point of the HTHH volcano, as shown in Fig. 8. The amplitude of the geomagnetic field oscillation at Honolulu was much smaller than at Apia. The amplitude difference could be due to the local time dependence on ionospheric conductivities (Iyemori et al. 2022). Iyemori et al. (2022) estimated the Pedersen and Hall conductivities to be 8.3 S and 12.6 S at Apia and 1.9 S and 3.2 S at Honolulu, respectively. However, because the observed amplitude difference cannot be explained only by the ionospheric conductivity difference, Iyemori et al. (2022) suggested that the geomagnetic longitudinal difference may also be one of the causes of the observed amplitude difference. The phase of the geomagnetic field oscillation at Honolulu is opposite to that at Apia. A possible mechanism of the anti-phase oscillation is shown in Fig. 9 (Iyemori et al. (2022)). In this figure, after the HTHH volcanic eruption, an eastward electric field is generated in the dynamo layer at an altitude of the E-region, and the field-aligned currents flow between the northern and southern hemispheres. Then, a polarization electric field accompanying the field-aligned currents is transmitted along the magnetic field lines to another hemisphere. The dynamo and polarization electric fields drive the Hall currents in both hemispheres, shown in Fig. 9. Because the Hall current direction is anti-parallel to each other on the left and right sides of the footprint of the field-aligned current, the phase of the observed geomagnetic field variations shows an anti-correlation, depending on the location of the geomagnetic observatories. Iyemori et al. (2022) and Yamazaki et al. (2022) interpreted that the geomagnetic field oscillations are caused by the effect of the ionospheric dynamo in the sunlit region. Thus, simultaneous detection of the geomagnetic field oscillations at magnetic conjugate points has not been reported before. Yamazaki et al. (2022) pointed out that modeling studies are essential for understanding the three-dimensional distribution of the ionospheric current caused by the HTHH volcanic eruption.

To give further confirmation and insight of the magnetic conjugate feature of 4-min oscillations reported

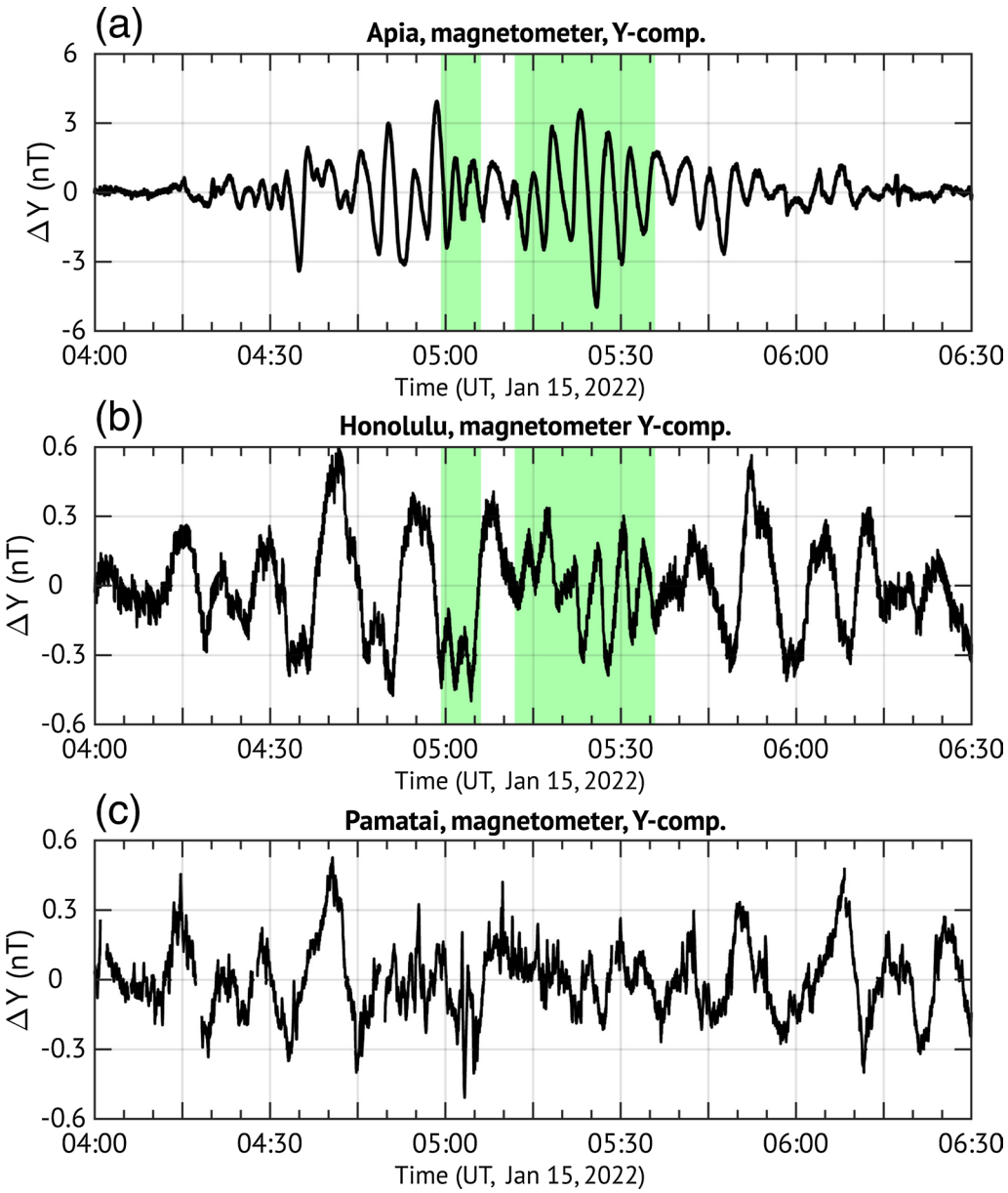

Fig. 8 High-pass filtered Y component of the geomagnetic field at Apia, Honolulu, and Pamatai with a cut-off frequency of ~ 0.8 mHz. The green boxes indicate the time interval where the waveform of ΔY at Honolulu is similar to that at Apia (Yamazaki et al. 2022)

by Iyemori et al. (2022) and Yamazaki et al. (2022), we analyzed the northward plasma flow observed by the SuperDARN Hokkaido east radar. The result is shown in Fig. 10. In this figure, two negative excursions of the northward plasma flows appeared with their amplitudes of approximately 100 m/s around 08:10 UT and 08:50 UT. These phenomena have already been reported by Shinbori et al. (2022). After the large plasma flow perturbations, the short-period oscillations were observed for approximately 20 min indicated by the horizontal red arrows. The average amplitude and period are 30 m/s and 4 min, respectively. The period of the northward plasma flow variations is almost consistent with that derived from different parameters (e.g., Iyemori et al. 2022). Therefore, it can be thought that the plasma flow oscillations are generated by the acoustic resonance triggered by the air pressure waves. In the range-time plots in Figs. 10a, c, e, the 4-min plasma flow oscillations tend to move in the direction of the decreasing range gate with time. This result indicates that the plasma flow

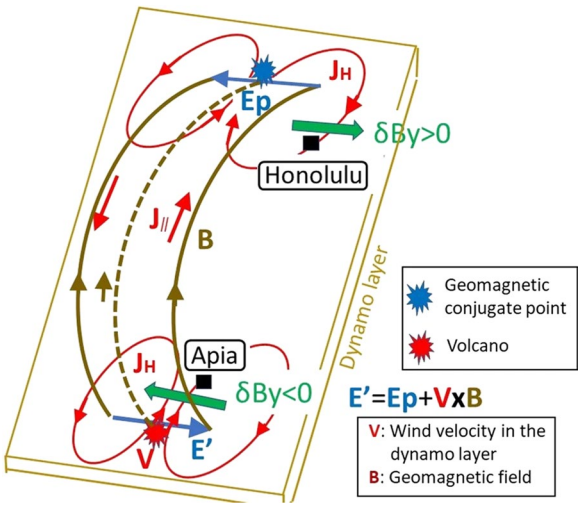

Fig. 9 A schematic view of the relationship among the HTHH volcanic eruption, geomagnetically conjugate point, inter-hemispheric field-aligned currents, electric field transmission, ionospheric Hall current, and magnetic effect on the ground. In this figure, the symbol 'V' represents the neutral wind velocity in the ionospheric dynamo layer (mainly E-layer) caused by the HTHH eruption. Ep and V × B indicate the polarization and Lorentz electric fields (Iyemori et al. 2022)

oscillations propagate westward when we consider that the beams-6, 7, and 8 of the SuperDARN Hokkaido east radar are directed in the north-east direction. The propagation direction is almost the same as that of the two main plasma flow variations reported by Shinbori et al. (2022). Considering the propagation feature and occurrence of the 4-min oscillations before the initial arrival of the air pressure wave to the FOV of the SuperDARN radar, the observed 4-min oscillations can be generated by a transmission of an electric field along the magnetic field line from the sunlit southern hemisphere as shown in a model of Shinbori et al. (2022). Because the magnetic field intensity and inclination at an altitude of the ionosphere (300 km) are calculated as 52,084.8 nT and 62.83 degrees with the IGRF-13 model, we can further estimate the eastward electric field of the 4-min oscillations as approximately 1.39 mV/m. This value is smaller than that of the two main plasma flow variations shown by Shinbori et al. (2022).

Appearance of an ionospheric hole over the HTHH volcano

Electron density depletions ("hole") in the ionosphere had been observed after large earthquakes such as the 2011 Tohoku-Oki earthquake (e.g., Astafyeva et al. 2013a, b; Kakinami et al. 2012). Astafyeva et al. (2013b) reported that the magnitude and duration of the ionospheric hole depend on the earthquake's magnitude and interpreted that the hole is generated by the rarefaction of the shock-acoustic waves triggered by earthquakes and tsunamis. For the 2011 Tohoku-Oki earthquake, the ionospheric hole was formed after 30–50 min, and the TEC value decreased by −5 to −6 TECU from the level before the earthquake (Astafyeva et al. 2013a, b). Such an ionospheric hole appeared with an amplitude of −18 to −13 TECU over the HTHH volcano after the large eruption. This phenomenon persisted for at least 1.5–2 h (Astafyeva et al. 2022). The huge ionospheric hole with a magnitude of more than 10 TECU extended around 2000 km away from the epicenter of the HTHH volcanic eruption (Aa et al. 2022a). Astafyeva et al. (2022) proposed that the HTHH volcanic eruption generated stronger shock waves with large amplitude and prolonged the rarefaction phase compared to those from other earthquakes. Aa et al. (2022a) indicated that the ionospheric hole consists of cascading TEC decreases associated with different acoustic waves.

Because the TEC value is an integration of electron density in the ionosphere along the path between the satellite and receiver on the ground, we cannot obtain information on the vertical profile of electron density and its variation from the GNSS-TEC observation. Further, we cannot investigate the temporal and spatial evolution of the TEC variation in most of the ocean areas due to the lack of ground-based receivers. To solve the above problems, Sun et al. (2022a) examined the electron density variations in the vertical direction associated with the HTHH volcanic eruption using the electron density profile obtained from the RO technique onboard the satellites of the FORMOSAT-7/COSMIC2 mission. Figure 11 shows the vertical profiles of the average electron density in the area near the epicenter of the HTHH volcanic eruption. In Fig. 10a, the peak value of the electron density is ~10×10^5 el/m^3, and the height of the peak value is ~330 km during 00:00–04:15 UT on 13–15 January. These electron density profiles are almost consistent with those under normal conditions before the HTHH volcanic eruption at 04:15 UT on 15 January. During 04:15–10:00 UT after the eruption, the electron density profile on 15 January shows a significant decrease above 250 km, compared with that on 13 and 15 (Fig. 11b). The F-region of the ionosphere almost disappeared and did not satisfy the usual Chapman layer (Davies 1990) anymore in the nighttime during 10:00–18:00 UT on 15 January (Fig. 11c). In Fig. 10d, the electron density profile on 15 January shows the recovery to reach the same level as that on other days after sunrise. Sun et al. (2022a) also showed that the disappearance of the F-region of the ionosphere with a horizontal scale of ~4000 km persisted for ~8 h over the HTHH volcano due to the eruption. However, it has been believed that the ionospheric hole is generated by the vertical motion

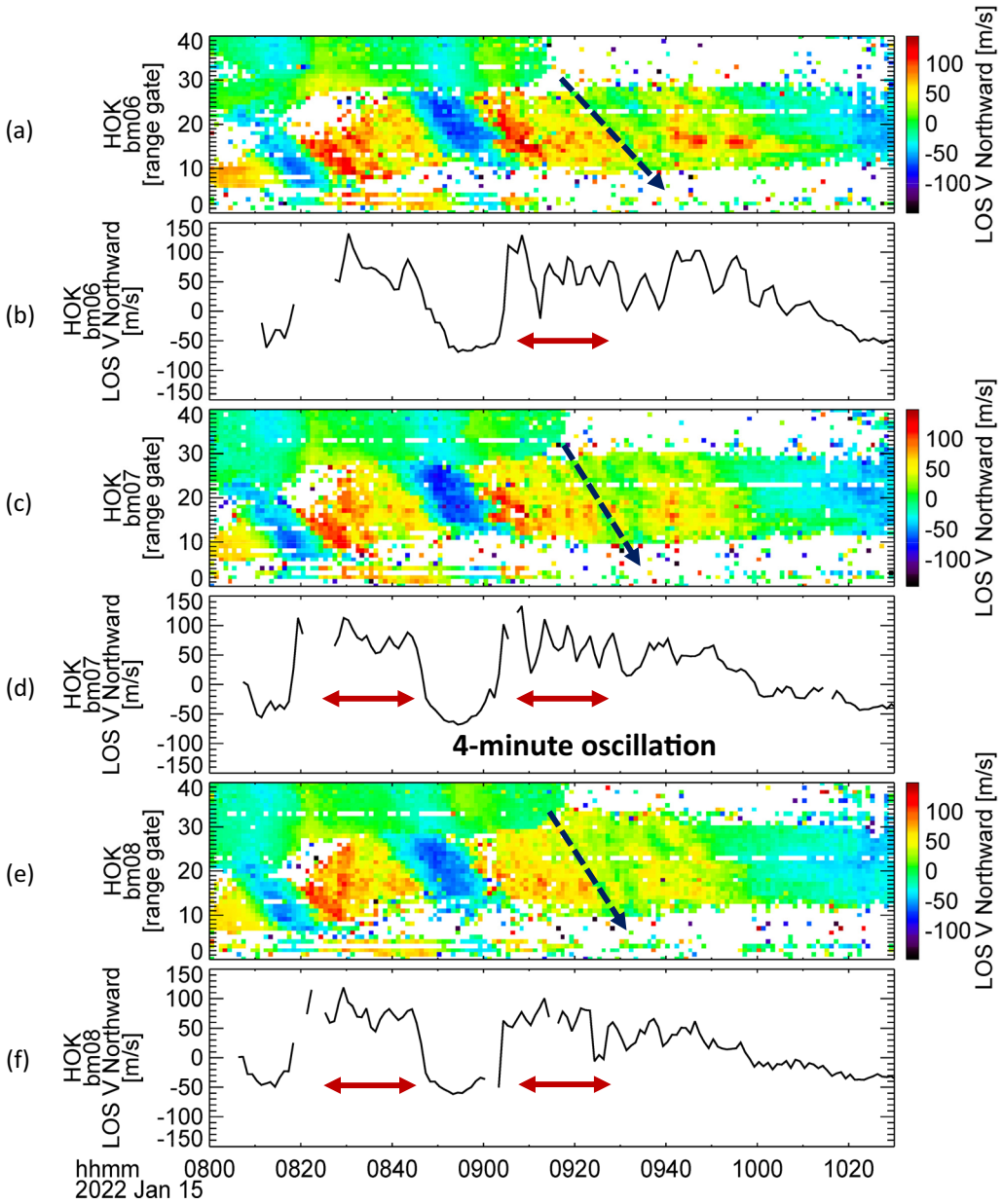

Fig. 10 Range-time plots of the northward plasma flow in the beam-6, 7, and 8 directions observed by the SuperDARN Hokkaido east radar (**a**, **c**, **e**). The color bar of each panel indicates the northward component of the line-of-site velocity in a range from − 150 to 150 m/s. Panels **b**, **d**, **f** show the time-series plots of the northward plasma flow at the range gate number of 17 in each beam. The horizontal red arrows in the panels **b**, **d**, **f** indicate the observed periods of 4-min oscillations. The phase variation of the 4-min oscillations for the range gate number is shown in the dashed blue arrows

of the neutral atmosphere due to earthquakes and tsunamis (Kakinami et al. 2012; Kakinami et al. 2012). The disappearance of the Chapman-layer structure was not identified in the case of the 2011 Tohoku earthquake (Liu et al. 2019). Therefore, we need to consider another process that may cause the disruption of the Chapman-layer structure associated with an explosive eruption. Sun et al. (2022a) proposed that the explosive eruption released the molecular particles up to the upper atmosphere, which reduced the ratio of the atomic and molecular densities (e.g., $[O]/[N_2]$) and increased the recombination process of ionospheric plasmas. This process seems to maintain the ionospheric hall or the disruption of the Chapman-layer structure for several hours after the HTHH volcanic eruption. Further, Sun et al. (2022a) concluded that the disappearance of the major ionospheric layers leads to the

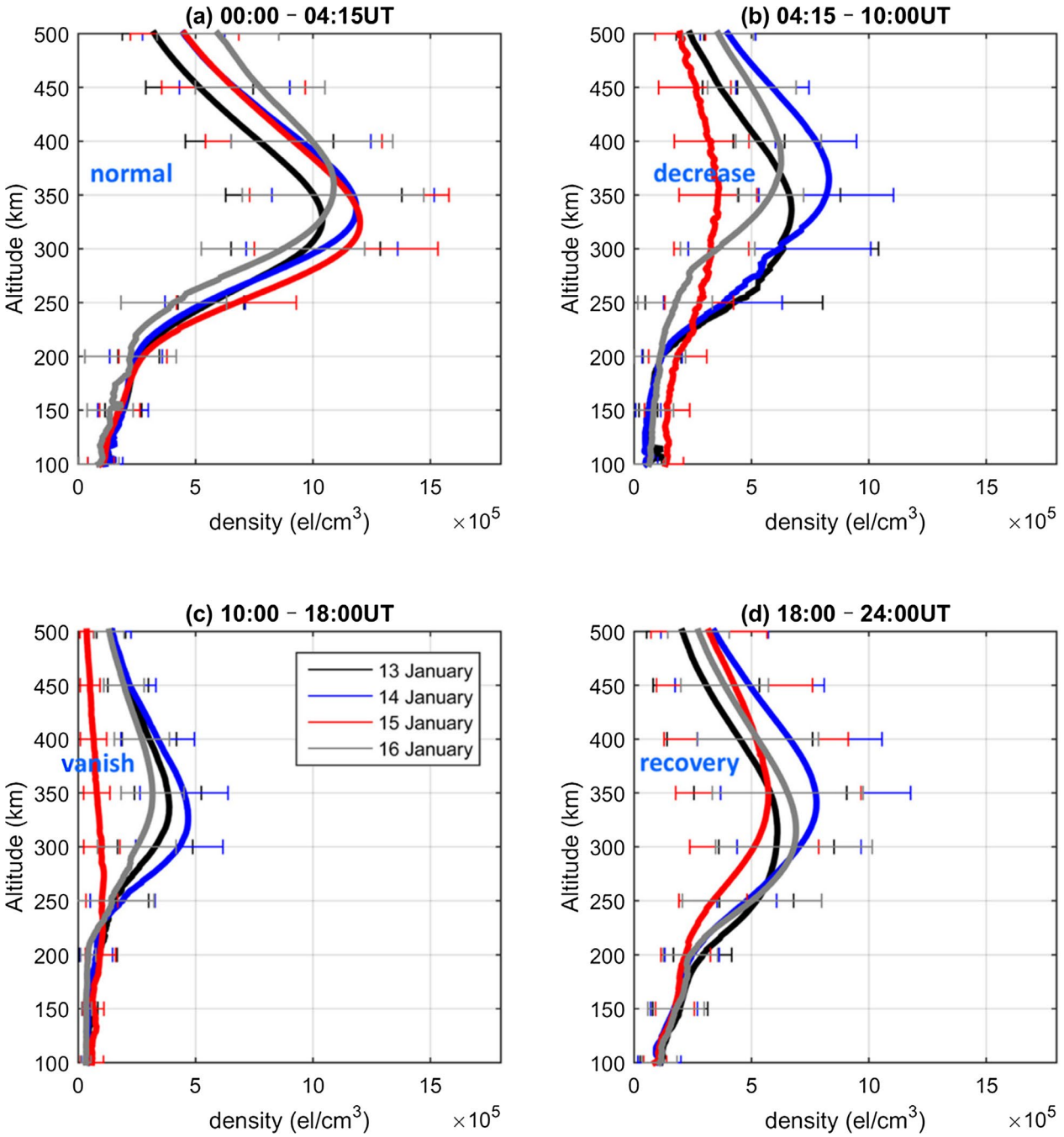

Fig. 11 Comparison of the average electron density profiles (**a**) before and **b**–**d** after the large HTHH volcanic eruption on 15 January and those on the two days before (13 and 14 January) and the one day after (16 January). The error bar indicates the standard deviation of the electron density at each altitude. The F2 layer vanished between 10:00 and 18:00 UT (Sun et al. 2022a, b, c)

electron density depression due to the explosive eruption of the HTHH volcano, which is much more effective than the 2011 Tohoku earthquake and tsunami for the upper atmosphere and ionosphere. Accelerometer data from the Gravity Recovery And Climate Experiment—Follow On (GRACE-FO) and Swarm-C observations showed that a large-scale neutral density depletion was formed within a radius of approximately 10,000 km around the epicenter and this structure persisted for a long time (Li et al. 2023a, b). The location of the neutral density depletion was almost consistent with that of the TEC depletion in the ionosphere (Aa et al. 2022a; Astafyeva et al.

2022). On the other hand, He et al. (2023) discussed the relative contributions of the HTHH eruption and the geomagnetic storm that occurred on 14 January 2022 before the HTHH eruption, based on an integrated analysis of GNSS-derived vertical TEC, O/N_2 ratio by Thermosphere, Ionosphere, Mesosphere Energetics and Dynamics (TIMED)/Global Ultraviolet Imager (GUVI), ion density and temperature by ICON/ion velocity meter (IVM), and—thermosphere ionosphere electrodynamics general circulation model (TIEGCM). Their results showed that the TEC near the HTHH volcano decreased by ~80–95% below the quiet-time values. Approximately 20 percent of the TEC depletion was caused by the thermospheric composition changes due to a moderate geomagnetic storm. In the future, the detailed physical mechanism of the formation of ionospheric holes should be examined with the atmosphere–ionosphere coupling model.

Generation of plasma bubbles in the equatorial and low-latitude ionosphere

Equatorial plasma bubble (EPB) is one of the ionospheric irregularities with a sharp plasma density depletion frequently observed in the nighttime equatorial and low-latitude ionosphere. The EPB is generated by the Rayleigh–Taylor (R–T) instability at the bottom side of the F-region. Atmospheric waves may seed the R–T instability. The growth rate of the R–T instability is enhanced by the prereversal enhancement (PRE) of the eastward electric field around the duskside terminator of the ionosphere (e.g., Kelley 2009; Abdu 2019). As the EPBs are developed, the region of plasma density depletion extends to higher altitudes through the polarization electric field inside the EPBs. The EPB structure is formed along the magnetic field lines and mapped to the low-latitude ionosphere away from the equator (Otsuka et al. 2002; Keskinen et al. 2003; Sori et al. 2022). The plasma density irregularity associated with the EPB causes signal fading, scintillation, and loss-of-lock in satellite-based communication and navigation systems in a wide region (e.g., Seo et al. 2009; Alfonsi et al. 2013). Therefore, it is essential to clarify the occurrence features of EPB to reduce the possible risks of the influence of radio wave propagation. Although the day-to-day variability of the EPB occurrence has not yet been fully understood due to the atmospheric and ionospheric conditions, including seeding sources and driving forces (e.g., Li et al. 2021), the explosive HTHH volcanic eruption provides us with an excellent opportunity to demonstrate that the EPB can be induced by lower atmospheric disturbances originating from the eruption.

For the first time, Aa et al. (2022a) found equatorial plasma troughs and EPBs with small-scale plasma density irregularities over the Asia-Oceania area after the HTHH volcanic eruption from ground-based GNSS-TEC and Swarm/ICON satellite observations. The onset time of an enhancement of the rate of the TEC index (ROTI) enhancement (Pi et al. 1997) that indicated the EPB occurrence was almost coincident with the arrival time of a Lamb wave at a speed of ~ 315 m/s. The ICON-IVM observation data showed upward plasma drifts of 60–120 m/s in the dusk sector, whose ionospheric motion creates one of the favorable conditions of the EPB generation (Aa et al. 2022a). Sun et al. (2022a, b, c) also reported the EPB occurrence at midlatitudes (up to ~ 35° in geographic latitude) over China after the passage of the sunset terminator at an E-region altitude (100 km). Further, Sun et al. (2022a, b, c) pointed out that the EPB occurrence associated with the HTHH volcanic eruption had three interesting aspects compared with that in a usual case. (1) Over the Asian sector, EPB is frequently observed in the equinox of solar maximum (e.g., Shi et al. 2011; Buhari et al. 2017). In the HTHH case, EPB was activated in the northern hemisphere's winter under the solar minimum condition, and the EPB occurrence was not recognized except for the HTHH eruption day (Shinbori et al. 2023) (2) The EPB usually tends to move eastward (e.g., Fejer et al. 2005), but the EPB associated with the HTHH volcanic eruption moved westward. (3) EPB is mainly observed at low latitudes within ±20° under the solar minimum condition (Li et al. 2021). However, in the HTHH case, the upper limit of the observed latitude of EPB extended to midlatitudes more than 30° N that can be categorized as super plasma bubbles (e.g., Aa et al. 2018; Cherniak and Zakharenkova 2016; Ma and Maruyama 2006; Rajesh et al. 2022; Shinbori et al. 2023). Shinbori et al. (2023) reported that the EPB observed over 100–150° E reached ~ 30° N in geomagnetic latitude after the initial arrival of the air pressure waves propagating in the troposphere (Fig. 12a). The apex altitude is estimated as ~ 3000 km. To confirm the EPB occurrence in the ionosphere, Shinbori et al. (2023) analyzed the electron density data derived from in-situ plasma waves (upper limit frequency of upper hybrid resonance (UHR) waves) observed by the plasma wave experiment (PWE)-high-frequency analyzer (HFA) instrument (Kumamoto et al. 2018) onboard the Arase satellite (Miyoshi et al. 2018a). For the derivation of the electron density data, Shinbori et al. (2023) used magnetic field data obtained from the Arase magnetic field (MGF) instrument (Matsuoka et al. 2018a). The electron density variation shows several depletions of one or two orders of magnitude after the rapid increase associated with the initial arrival of the air pressure waves (Fig. 12b). The occurrence region of electron density depletions is almost consistent with the enhanced ROTI region (Fig. 12c). In this case, the Arase

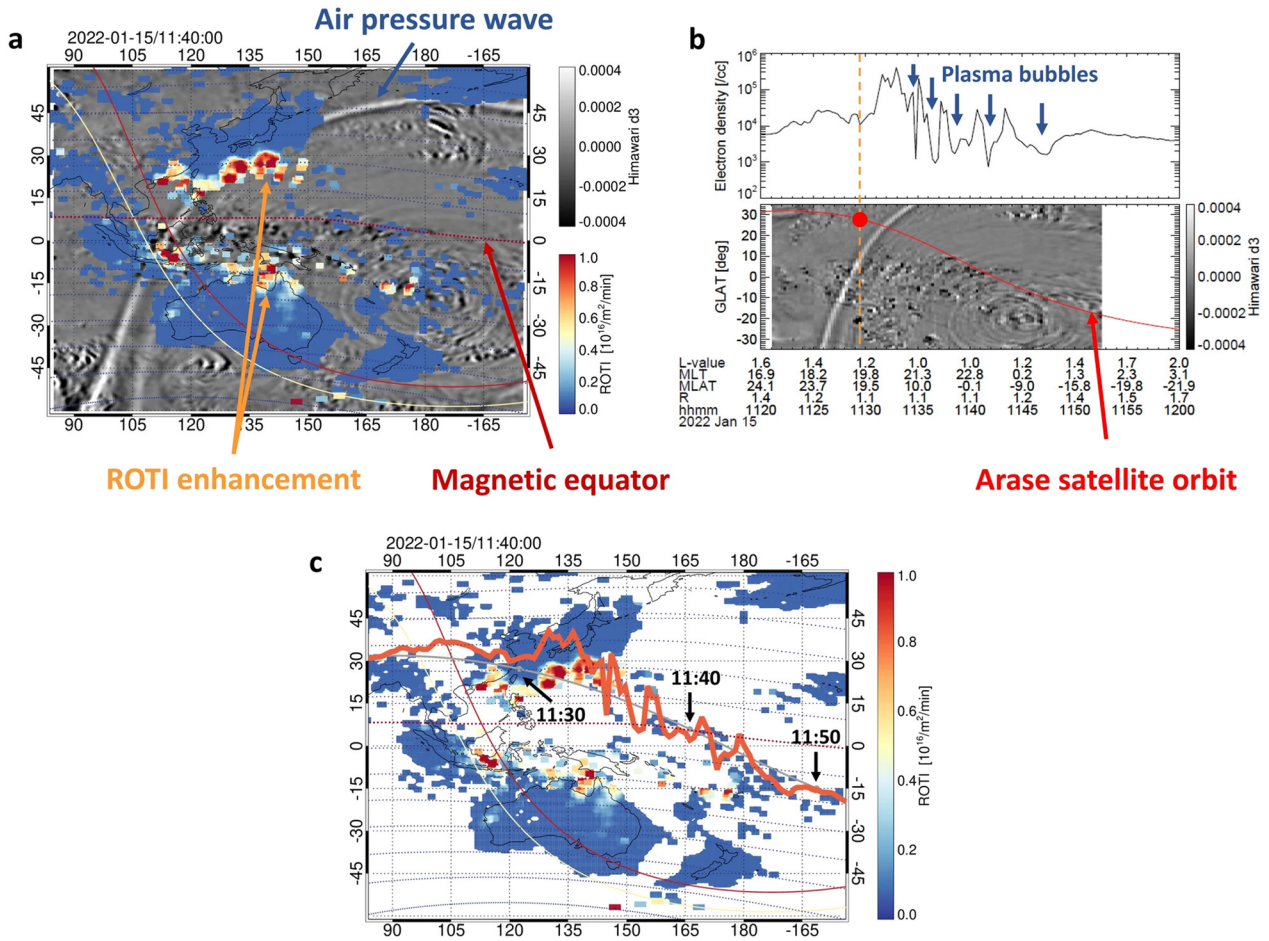

Fig. 12 Observation of the EPB and air pressure wave between 11:20 to 12:00 UT on 15 January 2022. **a** Two-dimensional map of ROTI and the Himawari-8 temperature deviation (d3) at 11:40 UT, indicated by the color and gray scales, respectively. The yellow and red lines represent the 105 and 300 km sunset terminators. The horizontal dashed curves show the geomagnetic latitude every 10°. **b** Electron density observed by the Arase satellite and geographic latitude-time plot of Himawari-8 d3 data along the geographic longitude of the Arase satellite location. **c** Two-dimensional map of ROTI with the electron density along the Arase satellite path in the same period as in Fig. 11b. The smoothed gray curve is the Arase satellite orbit, while the thick orange line around the smoothed curve is the electron density variation (Shinbori et al. 2023)

satellite traveled in the evening sector after the sunset terminator in the ionosphere, and the EPB was detected from 400 km (ionosphere) to at least 2000 km (low-altitude plasmasphere). Such super plasma bubbles could be caused by the combination of volcano-induced atmospheric perturbations (Shinbori et al. 2023) and strong PRE in the evening ionosphere (e.g., Rajesh et al. 2022).

To influence the propagation of electromagnetic waves in the ionosphere associated with the EPB, we investigated plasma wave dynamic spectra of the electric field component obtained from the PWE-HFA instrument onboard the Arase satellite. Figure 13 shows the plasma wave dynamic spectra in a frequency range from 3 kHz to 6 MHz when the Arase satellite encountered an air pressure wave propagating in the troposphere shown in Fig. 12b. In Fig. 13, a lot of narrow-banded line spectra appeared with a constant frequency for time above the UHR frequency indicated by the pink line after the encounter of the air pressure wave. These phenomena have been called the hectometric line spectra (HLS) (Hashimoto et al. 2018). The HLS in a frequency range from 1.0 to 1.5 MHz were trapped inside the electron density depletions corresponding to EPBs. Hashimoto et al. (2018) identified the origin of the HLS of the frequency component from 525 kHz to 1.7 MHz as amplitude modulation (AM) broadcasting waves propagating from the ground through the electron density depletions. Further, Hashimoto et al. (2021) confirmed that the HLS were frequently observed in the occurrence region of EPBs or low electron density region in the post-midnight sector using GNSS-TEC and Arase plasma wave observations. Therefore, appearance of such HLS in space found in the present study indicates that broadcasting waves in a wide frequency range escaped to space through

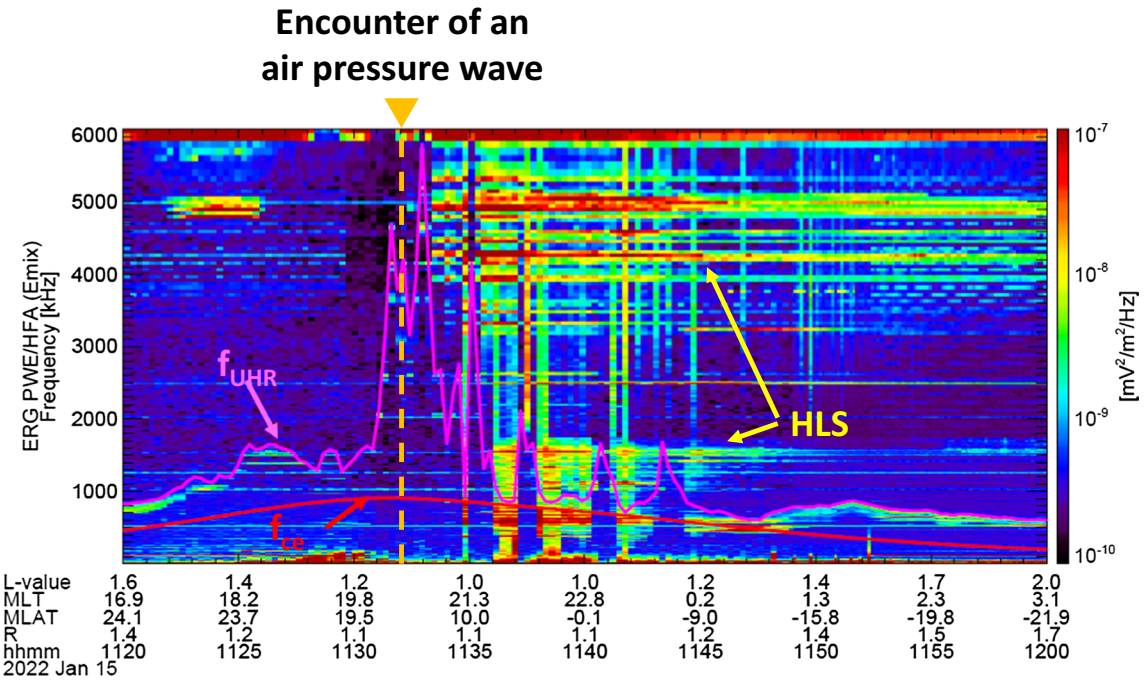

Fig. 13 Dynamic spectra of plasma waves in a frequency range from 3 to 6000 kHz obtained from the PWE-HFA instrument onboard the Arase satellite. The pink and red curves indicate the upper limit frequency of the UHR waves and the electron cyclotron frequency, respectively. The vertical dashed line is the time when the Arase satellite encountered an air pressure wave propagating in the troposphere. The right color bar shows the power spectrum of the electric field in a unite of $mV^2/m^2/Hz$

the low electron density region produced by the super plasma bubbles triggered by the HTHH volcanic eruption. Therefore, it can be considered that such super EPBs severely impacted the propagation of the HF broadcasting waves between the ground and ionosphere (Fig. 13).

Huba et al. (2023) investigated the impact of the HTHH volcanic eruption on the ionosphere and plasmasphere using the coupled SAMI3 model (Sami3 is also a model of the ionosphere/plasmasphere) and the high altitude mechanistic general circulation model (HIAMCM) whole atmosphere model in addition to primary gravity wave effects from the model for gravity wave sources, ray tracing and reconstruction (MESORAC) model. Their simulation results showed that the HTHH volcanic eruption generated a super EPB extending to ~30° in longitude and up to 500 km in altitude with an electron density depletion of 3 orders of magnitude. Further, Huba et al. (2023) found that the EPB reached high altitudes of more than 4000 km, which is much higher than that shown in previous simulation studies (e.g., Huba and Liu 2020). This result is consistent with the Arase satellite observation in space reported by Shinbori et al. (2023).

Carter et al. (2023) demonstrated the impacts of the HTHH volcanic eruption on the ionosphere and what subsequent impacts they had on precise point positioning (PPP) with a network of ionosondes located throughout the Australian region together with GNSS receivers. As a result, PPP accuracy was not significantly affected by the TIDs and Spread-F under the condition that PPP convergence had already been completed. However, when the PPP procedure was started either shortly before or after the TID arrivals, it took much more time (~5 h) to achieve the PPP convergence. Carter et al. (2023) also found that the convergence times were affected by a super EPB which is the largest phenomenon observed over Australia to date. It showed a depression of ~42 TECU and propagated eastwards at 30 m/s. Based on these results, Carter et al. (2023) concluded that the HTHH volcanic eruption was a good example of how ionospheric disturbances could adversely influence satellite-based precise positioning.

Discussion and conclusions

The explosive eruption of the HTHH undersea volcano occurred at 04:15 UT on 15 January 2022, and a vertical ash plume released by the HTHH volcanic eruption reached approximately 55 km, corresponding to the height of the lower mesosphere. The HTHH volcanic eruption generated acoustic waves, atmospheric gravity waves, strong shock waves, and air pressure waves (Lamb waves) to propagate in the troposphere. Furthermore, these atmospheric waves triggered tsunamis and

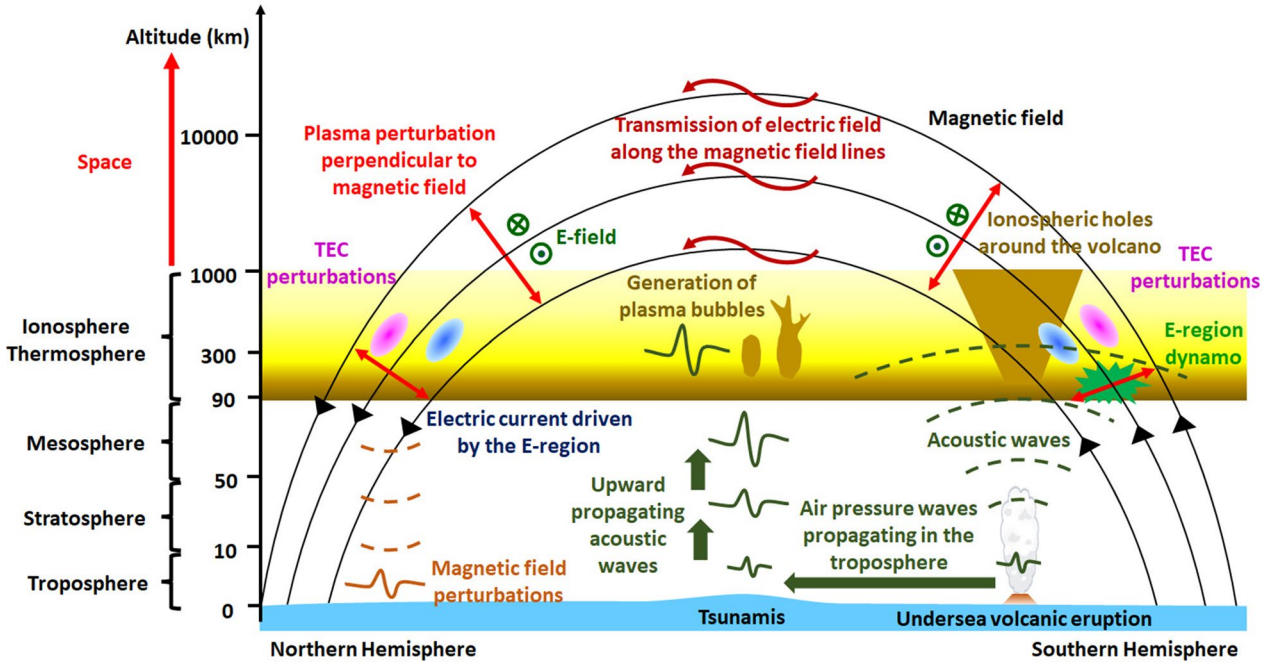

Fig. 14 Schematic view of the generation process of atmospheric and ionospheric disturbances observed after the explosive eruption of the HTHH volcano. The vertical axis in the left panel indicates the altitude and atmospheric layers

ionospheric disturbances detected by ground-based instruments worldwide. Such a global-scale atmospheric and ionospheric response to a large volcanic eruption had not yet been observed since the 1980s, when the global observation of the Earth's atmosphere and ionosphere started. Therefore, the HTHH volcanic eruption provides a unique opportunity to promote interdisciplinary studies of coupling processes in lithosphere–atmosphere–ionosphere with ground-based and satellite observations and modeling.

Through such interdisciplinary studies using various kinds of observation and simulation data, we could reveal the propagation feature and generation mechanisms of TIDs, the triggering mechanism of EPBs associated with the large-scale lower atmospheric disturbances, the cause of the electron density hole around the HTHH volcano, the modification of the plasma density structure of equatorial ionization anomaly (EIA), and the magnetic conjugacy of magnetic field perturbations. The most notable point among these studies is that the TIDs have magnetic conjugacy even in the daytime ionosphere and are generated by an external electric field, such as an E-region dynamo field, due to the motion of neutrals in the lower thermosphere. Jonah et al. (2017) also found that normal MSTIDs appeared in South America with magnetic conjugacy during the daytime and proposed that the MSTIDs were generated by the atmospheric gravity-induced electric fields transmitted to the other hemisphere. Therefore, these results advocate another generation mechanism of MSTIDs other than the oscillation of neutrals associated with atmospheric gravity waves. The TIDs which have magnetic conjugacy after the HTHH volcano eruption also show different feature from the electrified MSTIDs, which are frequently observed at middle latitudes during nighttime although both TIDs are caused by polarization electric fields (e.g. Otsuka 2021). For the case of the nighttime electrified MSTIDs, the electron density increase (decrease) coincides with westward (eastward) component of polarization electric fields. This indicates that the polarization electric fields both generates and are generated by the electron density perturbations. On the other hand, Shinbori et al. (2022) have shown that the electric field perturbations were ahead of the TEC perturbations associated with the TIDs after the HTHH volcanic eruption and suggest that the external electric fields are responsible for the TID generation. Further, we analyzed the GNSS-TEC and SuperDARN Hokkaido east radar data when the air pressure wave passed through the FOV of the SuperDARN radar to check whether or not the magnetic conjugate effect of the TIDs can occur in the dark region of both hemispheres. In the analysis, an enhancement of the northward plasma flow was found to occur with a timing that corresponds to the arrival of air pressure wave, but no clear signature of TEC perturbations was observed at the magnetic conjugate point in the southern hemisphere at that time. In this case, the

Hall and Pedersen conductivities in the dark region were much smaller than those in the sunlit region. This result suggests that the occurrence of the magnetic conjugate TIDs triggered by the air pressure waves requires a high ionospheric conductivity enough to drive an E-region dynamo due to the oscillation of neutrals in the thermosphere. This point gives a new insight of understanding the magnetic conjugate TIDs observed after the explosive eruption of the HTHH volcano. This is one of the three new points found by the present study.

The second new point found by the present analysis of the SuperDARN Hokkaido east radar data is an appearance of 4-min ionospheric plasma flow oscillations after the two large plasma flow disturbances reported by Shinbori et al. (2022). The plasma flow oscillations are generated by the acoustic resonances with their frequencies of 3.7 and 4.6 mHz (period of 3.5 and 4.5 min) (Kanamori and Mori 1992; Kanamori et al. 1994; Iyemori et al. 2005; Shinagawa et al. 2007). Using the SuperDARN radar to measure a two-dimensional distribution of ionospheric plasma flows (almost corresponding to ionospheric electric fields), the present study showed that the 4-min ionospheric plasma flow oscillations appeared in the northern hemisphere several hours before the air pressure waves arrived at the FOV of the SuperDARN radar. Further, it was found that the plasma flow oscillations propagated westward in the range-time plot of northward plasma flow (Fig. 10). The direction is consistent with that of the two large plasma flows generated by an external electric field transmitted to the northern hemisphere along the magnetic field lines. From these characteristics of the 4-min plasma flow oscillations, it can be concluded that the acoustic waves generated by the westward propagating air pressure waves drive an E-region dynamo in the sunlit hemisphere and that the dynamo electric fields transmitted to the northern hemisphere cause the 4-min plasma flow oscillations in the ionosphere.

The Arase satellite observation and high-resolution simulation revealed not only that the lower atmospheric disturbances, such as a volcanic eruption, become the seeds of the EPB generation but also that the EPB can grow beyond the ionosphere and reach the lower plasmasphere (2000–4800 km). In the present study, it was found that many HLS appeared above the UHR frequency after the Arase satellite encounter the air pressure wave triggered by the HTHH volcanic eruption. The HLS in a frequency range from 1.0 to 1.5 MHz were trapped inside the electron density depletions corresponding to EPBs. Considering that the origin of the HLS is the broadcasting waves propagating from the ground through EPB, appearance of such HLS in space found in the present study implies that the broadcasting waves escaped to space through the super plasma bubbles triggered by the HTHH volcanic eruption. Therefore, it can be said that such super plasma bubbles severely impacted the propagation of the HF broadcasting waves between the ground and ionosphere.

These above results suggest that the explosive eruption of the HTHH volcano had a significant impact on space, the ionosphere, and the atmosphere. Figure 14 summaries a schematic view of the generation process of atmospheric and ionospheric disturbances triggered by the explosive eruption of the HTHH volcano. From the viewpoint of studies of the coupling process of the atmosphere–ionosphere system, what we learned through the explosive eruption of the HTHH volcano suggests that we should pay attention to the connection with space at a higher altitude than the ionosphere for a cataclysmic natural phenomenon. Therefore, we need to include natural phenomena that occurred on the ground in space weather research focusing on the space environmental changes associated with solar activity and geomagnetic disturbances. On the other hand, scientific knowledge obtained from recent studies of coupling processes of lithosphere–atmosphere–ionosphere through the HTHH volcanic eruption helps to understand a new picture of heliospheric science to investigate space environmental changes associated with an eruption of an active volcano in the solar system. To achieve such frontier studies, we need to promote a strong collaboration with a wide range of research fields in geoscience, such as volcanology, meteorology, upper atmospheric physics, and plasma physics.

Acknowledgements

We used the Inter-university Upper atmosphere Observation NETwork (IUGONET) database (IUGONET Type-A) and data analysis software. The GNSS data collection and processing were performed using the National Institute of Information and Communications Technology Science Cloud. Himawari-8 gridded data are distributed by the Center for Environmental Remote Sensing, Chiba University, Japan. Science data of the Exploration of energization and Radiation in Geospace (ERG) (Arase) satellite were obtained from the ERG Science Center operated by the Institute of Space and Astronautical Science, Japan Aerospace Exploration Agency and Institute for Space-Earth Environmental Research, Nagoya University (https://ergsc.isee.nagoya-u.ac.jp/index.shtml.en). SuperDARN is a collection of radars funded by the national scientific funding agencies of Australia, Canada, China, France, Italy, Japan, Norway, South Africa, the United Kingdom, and the United States of America.

Author contributions

AS reviewed recent papers on ionospheric disturbances associated with the explosive eruption of the HTHH volcano, carried out a significant part of the data analysis, and wrote the manuscript. YO, MN, and SP gathered worldwide GNSS data and developed the method to derive GNSS-TEC and ROTI data used in this study together with AS, and TS, YO, SN, NN, and YM oversaw the production of the data sets and discussed their interpretations. TT developed the procedure to analyze TIR grid data from the Himawara-8 satellite and discussed the results. IS and YM oversaw the ERG project and discussed the interpretation of the event. YK led the development and operation of PWE with the contribution of SM, AK, and FT, SM contributed to the processing of the PWE data. AM led the development and operation of MGF. All authors read and approved the final manuscript.

Funding
This work was supported by a JSPS KAKENHI Grant No. 16H06286. The coauthor (Yuichi Otsuka) was also supported by a MEXT/JSPS KAKENHI Grant Nos. 15H05815, 16H06286, 16H05736 20H00197, 20H01959, 20K14546, JP21H01144, JSPS Bilateral Joint Research Projects no. JPJSBP120226504, and JSPS Core-to-Core Program, B. Asia-Africa Science Platforms. The coauthor (Nozomu Nishitani) was supported by a JSPS KAKENHI Grant Nos. 18KK0099 and 22H01284. The coauthor (Takuo Tsuda) was supported by a JSPS KAKENHI Grant No. 21H01144. The coauthor (Shoya Matsuda) was supported by a JSPS KAKENHI Grant No. 20K14546. The coauthor (Yoshizumi Miyoshi) was supported by a JSPS KAKENHI Grant No. 20H01959.

Availability of data and materials
The Receiver Independent Exchange Format data used for GNSS-TEC processing were provided by 50 data providers. These have been listed on the webpage of the GNSS-TEC database (http://stdb2.isee.nagoya-u.ac.jp/GPS/GPS-TEC/gnss_provider_list.html). The mainly contributed providers are GAGE (https://www.unavco.org/data/gps-gnss/gps-gnss.html), CDDIS (https://cddis.nasa.gov/archive/gnss/data/daily/, Noll 2010), CHAIN (http://chain.physics.unb.ca/chain/pages/data_download, Jayachandran et al. 2009), PNGA (http://www.geodesy.cwu.edu, Pacific Northwest Geodetic Array (PANGA) 1996), IBGE (http://geoftp.ibge.gov.br/informacoes_sobre_posicionamento_geodesico/rbmc/dados/), SOPAC (http://garner.ucsd.edu/pub/rinex/), GEONET (http://datahouse1.gsi.go.jp/terras/terras_english.html), GNNZ (https://www.geonet.org.nz/data/types/geodetic), RENAG (https://doi.org/10.15778/resif.rg, RESIF 2017), SONEL (https://www.sonel.org/-GPS-.html), LINZ (https://apps.linz.govt.nz/ftp/positionz), INGV (http://ring.gm.ingv.it/, INGV RING Working Group 2016), SWSBM (https://www.sws.bom.gov.au/World_Data_Centre/1/1), AFREF (http://afrefdata.org/), TLALOCNET (http://tlalocnet.udg.mx/tlalocnetgsac/), Northern California Earthquake Data Center (NCEDC 2014; https://ncedc.org/bard.overview.html), EUREF (https://www.epncb.oma.be/, Bruyninx et al. 2019), RAMSAC (https://www.ign.gob.ar/NuestrasActividades/Geodesia/RamsacDescargaRinex, Piñón et al. 2018), and BIGF (http://www.bigf.ac.uk/data_access.html). The common time SuperDARN data in CDF format (Hori et al. 2013) at HKW and HOK were obtained from the ERG Science Center operated by ISAS/JAXA and ISEE/Nagoya University (https://ergsc.isee.nagoya-u.ac.jp/index.shtml.en, Miyoshi et al. 2018b). The Himawari 8 satellite TIR grid data are provided by the CEReS, Chiba University (http://www.cr.chiba-u.jp/databases/GEO/H8_9/FD/index_en_V20190123.html). The F10.7 index was provided by Natural Resources Canada (https://spaceweather.gc.ca/forecast-prevision/solar-solaire/solarflux/sx-5-flux-en.php). The present study used PWE/HFA L2 v01_01 (Kasahara et al. 2018), PWE/HFA L3 v01_02 (Kasahara et al. 2021), MGF-L2 v03_03 (Matsuoka et al. 2018b), OBT L2 v03 (Miyoshi et al. 2018c), and OBT L3 v02 (Miyoshi et al. 2018d) data.

Declarations

Ethics approval and consent to participate
Not applicable.

Consent for publication
Not applicable.

Competing interests
The authors declare that they have no competing interests.

Author details
[1]Institute for Space-Earth Environmental Research, Nagoya University, Nagoya, Aichi 464-8601, Japan. [2]National Institute of Information and Communications Technology, Koganei, Tokyo 184-8795, Japan. [3]The University of Electro-Communications, Chofugaoka, Chofu, Tokyo 182-8585, Japan. [4]Department of Geophysics, Tohoku University, Aoba-ku, Sendai 980-8578, Japan. [5]Planetary Plasma and Atmospheric Research Center, Tohoku University, Aoba-ku, Sendai 980-8578, Japan. [6]Graduate School of Natural Science and Technology, Kanazawa University, Kakuma-machi, Kanazawa 920-1192, Japan. [7]Word Data Center for Geomagnetism, Graduate School of Science, Kyoto University, Sakyo-ku, Kyoto 606-8502, Japan. [8]Institute of Space and Astronautical Science, Japan Aerospace Exploration Agency, Chuou-ku, Sagamihara 252-5210, Japan.

Received: 28 June 2023 Accepted: 4 November 2023
Published online: 22 November 2023

References

Aa E, Huang W, Liu S, Ridley A, Zou S, Shi L, Chen Y, Shen H, Yuan T, Li J, Wang T (2018) Midlatitude plasma bubbles over China and adjacent areas during a magnetic storm on 8 September 2017. Space Weather 16:321–331. https://doi.org/10.1002/2017SW001776

Aa E, Zhang S-R, Erickson PJ, Vierinen J, Coster AJ, Goncharenko LP, Spicher A, Rideout W (2022a) Significant ionospheric hole and equatorial plasma bubbles after the 2022 Tonga volcano eruption. Space Weather 20:e2022SW003101. https://doi.org/10.1029/2022SW003101

Aa E, Zhang SR, Wang W, Erickson PJ, Qian L, Eastes R, Harding BJ, Immel TJ, Karan DK, Daniell RE, Coster AJ, Goncharenko LP, Vierinen J, Cai X, Spicher A (2022b) Pronounced suppression and X-pattern merging of equatorial ionization anomalies after the 2022 Tonga volcano eruption. J Geophys Res 127:e2022JA030527. https://doi.org/10.1029/2022JA030527

Abdu MA (2019) Day-to-day and short-term variabilities in the equatorial plasma bubble/spread F irregularity seeding and development. Prog Earth Planet Sci 6:11. https://doi.org/10.1186/s40645-019-0258-1

Afraimovich EL, Perevalova NP, Plotnikov AV, Uralov AM (2001) The shock-acoustic waves generated by the earthquakes. Ann Geophys 19:395–409. https://doi.org/10.5194/angeo-19-395-2001

Afraimovich EL, Astafyeva EI, Demyanov VV, Edemskiy IK, Gavrilyuk NS, Ishin AB et al (2013) A review of GPS/GLONASS studies of the ionospheric response to natural and anthropogenic processes and phenomena. J Space Weather Space Clim 3:A27. https://doi.org/10.1051/swsc/20130049

Alfonsi L, Spogli L, Pezzopane M, Romano V, Zuccheretti E, De Franceschi G, Cabrera MA, Ezquer RG (2013) Comparative analysis of spread-F signature and GPS scintillation occurrences at Tucumán, Argentina. J Geophys Res 118:4483–4502. https://doi.org/10.1002/jgra.50378

Aoyama T, Iyemori T, Nakanishi K, Nishioka M, Rosales D, Veliz O, Safor EV (2016) Localized field-aligned currents and 4-min TEC and ground magnetic oscillations during the 2015 eruption of Chile's Calbuco volcano. Earth Planets Space 68:1–9. https://doi.org/10.1186/s40623-016-0523-0

Artru J, Farges T, Lognonne P (2004) Acoustic waves generated from seismic surface waves: propagation properties determined from Doppler sounding observation and normal-modes modeling. Geophys J Int 158:1067–1077. https://doi.org/10.1111/j.1365-246X.2004.02377.x

Aryal S, Gan Q, Evans JS, Laskar FI, Karan DK, Cai X, Greer KR, Wang W, McClintock WE, Eastes RW (2023) Tongan volcanic eruption induced global-scale thermospheric changes observed by the GOLD mission. Geophys Res Lett 50:e2023GL103158. https://doi.org/10.1029/2023GL103158

Astafyeva E (2019) Ionospheric detection of natural hazards. Rev Geophys 57:1265–1288. https://doi.org/10.1029/2019RG000668

Astafyeva E, Shalimov S, Olshanskaya E, Lognonné P (2013a) Ionospheric response to earthquakes of different magnitudes: larger quakes perturb the ionosphere stronger and longer. Geophys Res Lett 40:1675–1681. https://doi.org/10.1002/grl.50398

Astafyeva E, Rolland L, Lognonné P, Khelfi K, Yahagi T (2013b) Parameters of seismic source as deduced from 1 Hz ionospheric GPS data: Case-study of the 2011 Tohoku-Oki event. J Geophys Res 118:5942–5950. https://doi.org/10.1002/jgra50556

Astafyeva E, Maletckii B, Mikesell TD, Munaibari E, Ravanelli M, Coisson P, Manta F, Rolland L (2022) The 15 January 2022 Hunga Tonga eruption history as inferred from ionospheric observations. Geophys Res Lett 49:e2022GL098827. https://doi.org/10.1029/2022GL098827

Blanc E (1985) Observations in the upper atmosphere of infrasonic waves from natural or artificial sources: a summary. Ann Geophys 3:673–688

Blanc E, le Pichon A, Ceranna L, Farges T, Marty J, Herry P (2010) Global scale monitoring of acoustic and gravity waves for the study of the atmospheric dynamics. In: Infrasound monitoring for atmospheric studies. Springer, Dordrecht, pp 647–664. https://doi.org/10.1007/978-1-4020-9508-5_21

Bór J, Bozóki T, Sátori G, Williams E, Behnke SA, Rycroft MJ, Buzás A, Silva HG, Kubicki M, Said R, Vagasky C, Steinbach P, André KS, Atkinson M (2023) Responses of the AC/DC global electric circuit to volcanic electrical activity in the Hunga Tonga–Hunga Ha'apai eruption on 15 January 2022. J Geophys Res 128:e2022JD038238. https://doi.org/10.1029/2022JD038238

Boyde B, Wood A, Dorrian G, Fallows RA, Themens D, Mielich J, Elvidge S, Mevius M, Zucca P, Dabrowski B, Krankowski A, Vocks C, Bisi M (2022) Lensing from small-scale travelling ionospheric disturbances observed using LOFAR. J Space Weather Space Clim 12:34. https://doi.org/10.1051/swsc/2022030

Bruyninx C, Legrand J, Fabian A, Pottiaux E (2019) GNSS metadata and data validation in the EUREF Permanent Network. GPS Solut 23:106. https://doi.org/10.1007/s10291-019-0880-9

Buhari SM, Abdullah M, Yokoyama T, Otsuka Y, Nishioka M, Hasbi AM, Bahari SA, Tsugawa T (2017) Climatology of successive equatorial plasma bubbles observed by GPS ROTI over Malaysia. J Geophys Res 122:2174–2184. https://doi.org/10.1002/2016JA023202

Cahyadi MN, Handoko EY, Rahayu RW, Heki K (2021) Comparison of volcanic explosions in Japan using impulsive ionospheric disturbances. Earth Planets Space 73:228. https://doi.org/10.1186/s40623-021001539-5

Calais E, Minster JB (1998) GPS, earthquakes, the ionosphere, and the space shuttle. Phys Earth Planetary Interiors 105:167–181. https://doi.org/10.1016/s0031-9201(97)00089-7

Calais E, Minster JB, Hofton M, Hedlin M (1998) Ionospheric signature of surface mine blasts from Global Positioning System measurements. Geophys J Int 132:191–202. https://doi.org/10.1046/j.1365-246x.998.00438.x

Campbell-Brown MA (2022) Nuclear-test monitor calls Tonga volcano blast 'Biggest thing that we've ever seen'. https://www.gpb.org/news/2022/01/21/nuclear-test-monitor-calls-tonga-volcano-blast-biggest-thing-weve-ever-seen

Carr JL, Horváth Á, Wu DL, Friberg MD (2022) Stereo plume height and motion retrievals for the record-setting Hunga Tonga–Hunga Ha'apai eruption of 15 January 2022. Geophys Res Lett 49:e2022GL098131. https://doi.org/10.1029/2022GL098131

Carter BA, Pradipta R, Dao T, Currie JL, Choy S, Wilkinson P, Maher P, Marshall R, Harima K, Huy ML, Chien TM, Ha TN, Harris TJ (2023) The ionospheric effects of the 2022 Hunga Tonga Volcano eruption and the associated impacts on GPS Precise Point Positioning across the Australian region. Space Weather 21:e2023SW003476. https://doi.org/10.1029/2023SW003476

Chen C-H, Sun Y-Y, Zhang X, Gao Y, Wang F, Lin K, Tang C-C, Huang R, Xu R, Liu J, Wang Y, Chen C (2022) Resonant signals in the lithosphere–atmosphere–ionosphere coupling. Sci Rep 12:14587. https://doi.org/10.1038/s41598-022-18887-1

Chen P, Xiong M, Wang R, Yao Y, Tang F, Chen H, Qiu L (2023) On the ionospheric disturbances in New Zealand and Australia following the eruption of the Hunga Tonga–Hunga Ha'apai volcano on 15 January 2022. Space Weather 21:e2022SW003294. https://doi.org/10.1029/2022SW003294

Cheng K, Huang YN (1992) Ionospheric disturbances observed during the period of Mount Pinatubo eruptions in June 1991. J Geophys Res 97:16995–17004. https://doi.org/10.1029/92JA01462

Cherniak I, Zakharenkova I (2016) First observations of super plasma bubbles in Europe. Geophys Res Lett 43:11137–11145. https://doi.org/10.1002/2016GL071421

Chou MY, Lin CCH, Yue J, Tsai HF, Sun YY, Liu JY, Chen CH (2017) Concentric traveling ionosphere disturbances triggered by Super Typhoon Meranti (2016). Geophys Res Lett 44:1219–1226. https://doi.org/10.1002/2016GL072205

Chum J, Sindelarova T, Koucka PK, Podolska K, Rusz J, Base J, Nakata H, Hosokawa K, Danielides M, Schmidt C, Knez L, Liu J-Y, Molina M, Fagre M, Katamzi-Joseph Z, Ohya H, Omori T, Lastovicka J, Buresova DO, Kouba D, Urbar J, Truhlık V (2023) Atmospheric and ionospheric waves induced by the Hunga eruption on 15 January 2022: Doppler sounding and infrasound. Geophys J Int 233:1429–1443. https://doi.org/10.10193/gii/ggac517

Cronin SJ, Brenna M, Smith IEM, Barker SJ, Tost M, Ford M, Tonga'onevai S, Kula T, Vaiomounga R (2017) New volcanic island unveils explosive past. Eos. https://doi.org/10.1029/2017EO076589

Dautermann T, Calais E, Lognonné P, Mattioli GS (2009a) Lithosphere–atmosphere–ionosphere coupling after the 2003 explosive eruption of the Soufriere Hills Volcano, Monserrat. Geophys J Int 179:1537–1546. https://doi.org/10.1111/j.1365-246X.2009.04390.x

Dautermann T, Calais E, Mattioli GS (2009b) Global Positioning System detection and energy estimation of the ionospheric wave caused by the 13 July 2003 explosion of the Soufrière Hills Volcano, Montserrat. J Geophys Res 114:B02202. https://doi.org/10.1029/2008JB005722

Davies K (1990) Ionospheric radio. Peregrinus, London. https://doi.org/10.1049/PBEW031E

Dorrian G, Fallows R, Wood A, Themens DR, Boyde B, Krankowski A, Bisi M, Dąbrowski B, Vocks C (2023) LOFAR observations of substructure within a traveling ionospheric disturbance at mid-latitude. Space Weather 21:e2022SW003198. https://doi.org/10.1029/2022SW003198

Fejer BG, Souza JR, Santos AS, Costa Pereira AE (2005) Climatology of F region zonal plasma drifts over Jicamarca. J Geophys Res 110:A12310. https://doi.org/10.1029/2005JA011324

Fritts DC, Alexander MJ (2003) Gravity wave dynamics and effects in the middle atmosphere. Rev Geophys 41:1003. https://doi.org/10.1029/2001RG000106

Garvin JB, Slayback DA, Ferrini V, Frawley J, Giguere, Asrar GR, Andersen K (2018) Monitoring and modeling the rapid evolution of Earth's newest volcanic island: Hunga Tonga Hunga Ha'apai (Tonga) using high spatial resolution satellite observations. Geophys Res Lett 45:3445–3452. https://doi.org/10.1002/2017GL076621

Garvin JB (2022) Dramatic changes at Hunga Tonga–Hunga Ha'apai. https://earthobservatory.nasa.gov/images/149367/dramatic-changes-at-hungatonga-hunga-334

Gasque LC, Wu Y-J, Harding BJ, Immel TJ, Triplett CC (2022) Rapid volcanic modification of the E-region dynamo: ICON's first glimpse of the Tonga eruption. Geophys Res Lett 49:e2022GL100825. https://doi.org/10.1029/2022GL100825

Gavrilov BG, Poklad YV, Ryakhovsky IA, Ermak VM, Achkasov NS, Kozakova EN (2022) Global electromagnetic disturbances caused by the eruption of the Tonga volcano on 15 January 2022. J Geophys Res 127:e2022JD037411. https://doi.org/10.1029/2022JD037411

Ghent JN, Crowell BW (2022) Spectral characteristics of ionospheric disturbances over the southwestern Pacific from the 15 January 2022 Tonga eruption and tsunami. Geophys Res Lett 49:e2022GL100145. https://doi.org/10.1029/2022GL100145

Han S-C, McClusky S, Mikesell TD, Rolland L, Okal E, Benson C (2023) CubeSat GPS observation of traveling ionospheric disturbances after the 2022 Hunga-Tonga Hunga-Ha'apai volcanic eruption and its potential use for tsunami warning. Earth Space Sci 10:e2022EA002586. https://doi.org/10.1029/2022EA002586

Harding BJ, Wu Y-JJ, Alken P, Yamazaki Y, Triplett CC, Immel TJL, Gasque C, Mende SB, Xiong C (2022) Impacts of the January 2022 Tonga volcanic eruption on the ionospheric dynamo: ICON-MIGHTI and Swarm observations of extreme neutral winds and currents. Geophys Res Lett 49:e2022GL098577. https://doi.org/10.1029/2022GL098577

Hargreaves JK (1992) The solar-terrestrial environment. An introduction to geospace—the science of the terrestrial upper atmosphere, ionosphere and magnetosphere. Cambridge University Press, New York, p 436. https://doi.org/10.1017/CBO9780511628924

Hasbi AM, Momani MA, Ali MAM, Misran N, Shiokawa K, Otsuka Y, Yumoto K (2009) Ionospheric and geomagnetic disturbances during the 2005 Sumatran earthquakes. J Atmos Sol Terr Phys 71:1992–2005. https://doi.org/10.1016/j.jastp.2009.09.004

Hashimoto K, Kumamoto A, Tsuchiya F, Kasahara Y, Matsuoka A (2018) Hectometric line spectra detected by the Arase (ERG) satellite. Geophys Res Lett 45:11555–11561. https://doi.org/10.1029/2018GL080133

Hashimoto K, Shinbori A, Otsuka Y, Tsuchiya F, Kumamoto A, Kasahara Y, Matsuoka A, Nagano I, Miyoshi Y, Yokoyama T (2021) Propagation mechanism of medium wave broadcasting waves observed by the Arase satellite: hectometric line spectra. J Geophys Res 126:e2021JA029813. https://doi.org/10.1029/2021JA029813

He J, Astafyeva E, Yue X, Ding F, Maletckii B (2023) The giant ionospheric depletion on 15 January 2022 around the Hunga Tonga–Hunga Ha'apai volcanic eruption. J Geophys Res 128:e2022JA030984. https://doi.org/10.1029/2022JA030984

Heki K (2006) Explosion energy of the 2004 eruption of the Asama volcano, central Japan, inferred from ionospheric disturbances. Geophys Res Lett 33:L14303. https://doi.org/10.1029/2006GL026249
Heki K (2022) Ionospheric signatures of repeated passages of atmospheric waves by the 2022 Jan. 15 Hunga Tonga–Hunga Ha'apai eruption detected by QZSS-TEC observations in Japan. Earth Planets Space 74:112. https://doi.org/10.1186/s40623-022-01674-7
Heki K, Fujimoto T (2022) Atmospheric modes excited by the 2021 August eruption of the Fukutoku-Okanoba volcano, Izu-Bonin Arc, observed as harmonic TEC oscillations by QZSS. Earth Planets Space 74:27. https://doi.org/10.1186/s40623-022-01587-5
Heki K, Ping J (2005) Directivity and apparent velocity of the coseismic ionospheric disturbances observed with a dense GPS array. Earth Planet Sci Lett 236:845–855. https://doi.org/10.1016/j.epsl.2005.06.010
Hines CO (1960) Internal atmospheric gravity waves at ionospheric heights. Can J Phys 38:1441–1481. https://doi.org/10.1139/p60-150
Hong J, Kil H, Lee WK, Kwak Y-S, Choi B-K, Paxton LJ (2022) Detection of different properties of ionospheric perturbations in the vicinity of the Korean Peninsula after the Hunga-Tonga volcanic eruption on 15 January 2022. Geophys Res Lett 49:e2022GL099163. https://doi.org/10.1029/2022GL099163
Hori T, Nishitani N, Miyoshi Y, Miyashita Y, Seki K, Segawa T, Hosokawa K, Yukimatsu AS, Tanaka Y, Sato N, Kunitake M, Nagatsuma T (2013) An integrated analysis platform merging SuperDARN data within the THEMIS tool developed by ERG-Science Center (ERG-SC). Adv Polar Sci 24:69–77. https://doi.org/10.3724/SPJ.1085.2013.00069
Huang CY, Helmboldt JF, Park J, Pedersen TR, Willemann R (2019) Ionospheric detection of explosive events. Rev Geophys 57:78–105. https://doi.org/10.1029/2017RG000594
Huba JD, Liu H-L (2020) Global modeling of equatorial spread F with SAMI3/WACCM-X. Geophys Res Lett 47:e2020GL088258. https://doi.org/10.1029/2020GL088258
Huba JD, Becker E, Vadas SL (2023) Simulation study of the 15 January 2022 Tonga event: development of super equatorial plasma bubbles. Geophys Res Lett 50:e2022GL101185. https://doi.org/10.1029/2022GL101185
Inchin P, Heale C, Snively J, Zettergren M (2020) The dynamics of nonlinear atmospheric acoustic-gravity waves generated by tsunamis over realistic bathymetry. J Geophys Res 125:e2020JA028309. https://doi.org/10.1029/2020ja028309
INGV RING Working Group (2016) Rete Integrata Nazionale GNSS (2016). https://doi.org/10.13127/RING
Iyemori T, Nose M, Han D, Gao Y, Hashizume M, Choosakul N, Shinagawa H, Tanaka Y, Utsugi M, Saito A, McCreadie H, Odagi Y, Yang F (2005) Geomagnetic pulsations caused by the Sumatra earthquake on December 26, 2004. Geophys Res Lett 32:L20807. https://doi.org/10.1029/2005gl024083
Iyemori T, Nishioka M, Otsuka Y, Shinbori A (2022) A confirmation of vertical acoustic resonance and field-aligned current generation just after the 2022 Hunga Tonga Hunga Ha'apai volcanic eruption. Earth Planets Space 74:103. https://doi.org/10.1186/s40623-022-01653-y
Jayachandran PT, Langley RB, MacDougall JW, Mushini SC, Pokhotelov D, Hamza AM, Mann IR, Milling DK, Kale ZC, Chadwick R, Kelly T, Danskin DW, Carrano CS (2009) The Canadian high arctic ionospheric network (CHAIN). Radio Sci 44:RS0A03. https://doi.org/10.1029/2008RS004046
Jonah OF, Kherani EA, De Paula ER (2017) Investigations of conjugate MSTIDS over the Brazilian sector during daytime. J Geophys Res 122:9576–9587. https://doi.org/10.1002/2017JA024365
Kakinami Y, Kamogawa M, Tanioka Y, Watanabe S, Gusman AR, Liu JY, Watanabe Y, Mogi T (2012) Tsunamigenic ionospheric hole. Geophys Res Lett 39:L00G27. https://doi.org/10.1029/2011GL050159
Kanamori H, Mori J (1992) Harmonic excitation of mantle Rayleigh waves by the 1991 eruption of Mount Pinatubo, Philippines. Geophys Res Lett 19:721–724. https://doi.org/10.1029/92GL00258
Kanamori H, Mori J, Harkrider DG (1994) Excitation of atmospheric oscillations by volcanic eruptions. J Geophys Res 99:21947–21961. https://doi.org/10.1029/94jb01475
Kasahara Y, Kumamoto A, Tsuchiya F, Matsuda S, Shoji M, Nakamura S, Kitahara M, Shinohara I, Miyoshi Y (2018) The PWE/HFA instrument Level-2 spectrum data of exploration of energization and radiation in geospace (ERG) Arase satellite. https://doi.org/10.34515/DATA.ERG-10000
Kasahara Y, Kumamoto A, Tsuchiya F, Kojima H, Matsuda S, Matsuoka A, Teramoto M, Shoji M, Nakamura S, Kitahara M, Maeda A, Miyoshi Y, Shinohara I (2021) The PWE/HFA instrument Level-3 electron density data of exploration of energization and radiation in geospace (ERG) Arase satellite. https://doi.org/10.34515/DATA.ERG-10001
Kelley M (2009) The Earth's ionosphere: plasma physics and electrodynamics, 2nd edn. California Academic Press, San Diego
Keskinen MJ, Ossakow SL, Fejer BG (2003) Three-dimensional nonlinear evolution of equatorial ionospheric spread-F bubbles. Geophys Res Lett 30:1855. https://doi.org/10.1029/2003GL017418
Kong Q, Li C, Shi K, Guo J, Han J, Wang T, Bai Q, Chen Y (2023) Global ionospheric disturbance propagation and vertical ionospheric oscillation triggered by the 2022 Tonga volcanic eruption. Atmosphere 13:1697. https://doi.org/10.3390/atmos13101697
Koyama Y, Shinbori A, Tanaka Y, Hori T, Nosé M, Oimatsu S (2014) An Interactive Data Language software package to calculate ionospheric conductivity by using numerical models. Comput Phys Commun 185:3398–3405. https://doi.org/10.1016/j.cpc.2014.08.011
Kubota T, Saito T, Nishida K (2022) Global fast-traveling tsunamis driven by atmospheric Lamb waves on the 2022 Tonga eruption. Science 377:91–94. https://doi.org/10.1126/science.abo4364
Kulichkov SN, Chunchuzov IP, Popov OE, Gorchakov GI, Mishenin AA, Perepelkin VG, Bush GA, Skorokhod AI, Vinogradov YA, Semutnikova EG, Šepic J, Medvedev IP, Gushchin RA, Kopeikin VM, Belikov IB, Gubanova DP, Karpov AV, Tikhonov AV (2022) Acoustic-gravity Lamb waves from the eruption of the Hunga-Tonga–Hunga-Hapai volcano, Its energy release and impact on aerosol concentrations and tsunami, *Pure Appl*. Geophys 179:1533–1548. https://doi.org/10.1007/s00024-022-03046-4
Kumamoto A, Tsuchiya F, Kasahara Y, Kasaba Y, Kojima H, Yagitani S, Ishisaka K, Imachi T, Ozaki M, Matsuda S, Shoji M, Matsuoka A, Katoh Y, Miyoshi Y, Obara T (2018) High frequency analyzer (HFA) of plasma wave experiment (PWE) onboard the Arase spacecraft. Earth Planets Space 70:82. https://doi.org/10.1186/s40623-018-0854-0
Kundu B, Senapati B, Burgmann R, Ray S (2023) Detecting the 2022 January 15 Hunga Tonga–Hunga–Ha'apai volcanic eruption (SW Pacific) high up in the sky through 'ionospheric resonance.' Geophys J Int 233:922–931. https://doi.org/10.10193/gji/ggac492
Le G, Liu G, Yizengaw E, Englert CR (2022) Intense equatorial electrojet and counter electrojet caused by the 15 January 2022 Tonga volcanic eruption: space- and ground-based observations. Geophys Res Lett 49:e2022GL099002. https://doi.org/10.1029/2022GL099002
Li G, Ning B, Otsuka Y, Abdu M, Abadi P, Liu Z, Spogli L, Wan W (2021) Challenges to equatorial plasma bubble and ionospheric scintillation short-term forecasting and future aspects in east and southeast Asia. Surv Geophys 42:201–238. https://doi.org/10.1007/s10712-020-09613-5
Li X, Ding F, Yue X, Mao T, Xiong B, Song Q (2023a) Multiwave structure of traveling ionospheric disturbances excited by the Tonga volcanic eruptions observed by a dense GNSS network in China. Space Weather 21:e2022SW003210. https://doi.org/10.1029/2022SW003210
Li R, Lei J, Kusche J, Dang T, Huang F, Luan X, Zhang S-R, Yan M, Yang Z, Liu F, Dou Z (2023b) Large-scale disturbances in the upper thermosphere induced by the 2022 Tonga volcanic eruption. Geophys Res Lett 50:e2022GL102265. https://doi.org/10.1029/2022GL102265
Lin J-T, Rajesh PK, Lin CCH, Chou M-Y, Liu J-Y, Yue J, Hsiao T-Y, Tsai H-F, Chao H-M, Kung M-M (2022) Kung, Rapid conjugate appearance of the giant ionospheric lamb wave signatures in the Northern Hemisphere after Hunga-Tonga volcano eruptions. Geophys Res Lett 49:e2022GL098222. https://doi.org/10.1029/2022GL098222
Liu J-Y, Chen C-Y, Sun Y-Y, Lee I-T, Chum J (2019) Fluctuations on vertical profiles of the ionospheric electron density perturbed by the 11 March, 2011 M9.0 Tohoku earthquake and tsunami. GPS Solut 23:76. https://doi.org/10.1007/s10291-019-0866-7
Liu L, Morton YJ, Cheng P-H, Amores A, Wright CJ, Hoffmann L (2023) Concentric traveling ionospheric disturbances (CTIDs) triggered by the 2022 Tonga volcanic eruption. J Geophys Res 128:e2022JA056. https://doi.org/10.1029/2022JA56
Lognonné P, Clévédé E, Kanamori H (1998) Computation of seismograms and atmospheric oscillations by normal-mode summation for a spherical Earth model with realistic atmosphere. Geophys J Int 135:388–406. https://doi.org/10.1046/j.1365-246x.1998.00665.x

Ma G, Maruyama T (2006) A super bubble detected by dense GPS network at East Asian longitudes. Geophys Res Lett 33:L21103. https://doi.org/10.1029/2006GL027512

Madonia P, Bonaccorso A, Bonforte A, Buonocunto C, Cannata A, Carleo L, Cesaroni C, Currenti G, De Gregorio S, Di Lieto B, Guerra M, Orazi M, Pasotti L, Peluso R, Pezzopane M, Restivo V, Romano P, Sciotto M, Spogli L (2023) Propagation of perturbations in the lower and upper atmosphere over the Central Mediterranean, driven by the 15 January 2022 Hunga Tonga–Hunga Ha'apai volcano explosion. Atmosphere 14:65. https://doi.org/10.3390/atmos14010065

Maeda K, Kato S (1966) Electrodynamics of the ionosphere. Space Sci Rev 5:57–79. https://doi.org/10.1007/bf00179215

Maletckii B, Astafyeva E (2022) Near-real-time analysis of the ionospheric response to the 15 January 2022 Hunga Tonga–Hunga Ha'apai volcanic eruption. J Geophys Res 127:e2022JA030735. https://doi.org/10.1029/2022JA030735

Manta F, Occhipinti G, Hill E, Perttu A, Taisne B (2021) Correlation between GNSS-TEC and eruption magnitude supports the use of ionospheric sensing to complement volcanic hazard assessment. J Geophys Res 126:e2020JB020726. https://doi.org/10.1029/2020JB020726

Matoza RS, Fee D, Assink JD, Iezzi AM, Green DN, Kim K, Toney L, Lecocq T, Krishnamoorthy S, Lalande J-M, Nishida K, Gee KL, Haney MM, Ortiz HD, Brissaud Q, Martire L, Rolland L, Vergados P, Nippress A, Park J, Shani-Kadmiel S, Witsil A, Arrowsmith S, Caudron C, Watada S, Perttu AB, Mialle TP, La Pichon A, Vergoz J, Hupe P, Blom-Waxler R, de Angelis S, Snively JB, Ringler AT, Anthony RE, Jolly AD, Kilgour G, Averbuch G, Ripepe M, Ichihara M, Arciniega-Ceballos A, Astafyeva E, Ceranna L, Cevuard S, Che I-Y, de Negri R, Ebeling CW, Evers LG, Franco-Marin LE, Gabrielson TB, Hafner K, Harrison RG, Komjathy A, Lacanna G, Lyons J, Macpherson KA, Marchetti E, McKee KF, Mellors RJ, Mendo-Pérez G, Mikesell TD, Munaibari E, Oyola-Merced M, Park I, Pilger C, Ramos C, Ruiz MC, Sabatini R, Schwaiger HF, Tailpied D, Talmadge C, Vidot J, Webster J, Wilson DC (2022) Atmospheric waves and global seismoacoustic observations of the January 2022 Hunga eruption, Tonga. Science 377:95–100. https://doi.org/10.1126/science.abo7063

Matsumura M, Saito A, Iyemori T, Shinagawa H, Tsugawa T, Otsuka Y, Nishioka M, Chen CH (2011) Numerical simulations of atmospheric waves excited by the 2011 off the Pacific coast of Tohoku Earthquake. Earth Planets Space 63:885–889. https://doi.org/10.5047/eps.2011.07.015

Matsumura M, Shinagawa H, Iyemori T (2012) Horizontal extension of acoustic resonance between the ground and the lower thermosphere. J Atmos Sol Terr Phys 75:127–132. https://doi.org/10.1016/j.jastp.2011.12.003

Matsuoka A, Teramoto M, Nomura R, Nosé M, Fujimoto A, Tanaka Y, Shinohara M, Nagatsuma T, Shiokawa K, Obana Y, Miyoshi Y, Mita M, Takashima T, Shinohara I (2018a) The ARASE (ERG) magnetic field investigation. Earth Planets Space 70:43. https://doi.org/10.1186/s40623-018-0800-1

Matsuoka A, Teramoto M, Imajo S, Kurita S, Miyoshi Y, Shinohara I (2018b) The MGF instrument Level-2 high-resolution magnetic field data of Exploration of energization and Radiation in Geospace (ERG) Arase satellite. https://doi.org/10.34515/DATA.ERG-06000

Meng X, Vergados P, Komjathy A, Verkhoglyadova O (2019) Upper atmospheric responses to surface disturbances: an observational perspective. Radio Sci 54:1076–1098. https://doi.org/10.1029/2019RS006858

Mezentsev A, Nickolaenko AP, Shvets AV, Galuk YP, Schekotov AY, Hayakawa M, Romero R, Izutsu J, Kudintseva IG (2023) Observational and model impact of Tonga volcano eruption on Schumann resonance. J Geophys Res 128:1. https://doi.org/10.1029/2022JD037841

Miyoshi Y, Shinohara I, Takashima T, Asamura K, Higashio N, Mitani T, Kasahara S, Yokota S, Kazama Y, Wang S-Y, Tam SWY, Ho PTP, Kasahara Y, Kasaba Y, Yagitani S, Matsuoka A, Kojima H, Katoh Y, Shiokawa K, Seki K (2018a) Geospace exploration project ERG. Earth Planets Space 70:101. https://doi.org/10.1186/s40623-018-0862-0

Miyoshi Y, Hori T, Shoji M, Teramoto M, Chang TF, Segawa T, Umemura N, Matsuda S, Kurita S, Keika K, Miyashita Y, Seki K, Tanaka Y, Nishitani N, Kasahara S, Yokota S, Matsuoka A, Kasahara Y, Asamura K, Takashima T, Shinohara I (2018b) The ERG science center. Earth Planes Space 70:96. https://doi.org/10.1186/s40623-018-0867-8

Miyoshi Y, Shinohara I, Jun C-W (2018c) The Level-2 orbit data of Exploration of energization and Radiation in Geospace (ERG) Arase satellite. https://doi.org/10.34515/DATA.ERG-12000

Miyoshi Y, Shinohara I, Jun C-W (2018d) The Level-3 orbit data of Exploration of energization and Radiation in Geospace (ERG) Arase satellite. https://doi.org/10.34515/DATA.ERG-12001

Muafiry IN, Meilano I, Heki K, Wijaya DD, Nugraha KA (2022) Ionospheric disturbances after the 2022 Hunga Tonga–Hunga Ha'apai eruption above Indonesia from GNSS-TEC observations. Atmosphere 13:1615. https://doi.org/10.3390/atmos13101615

Munaibari E, Rolland L, Sladen A, Delouis B (2023) Anatomy of the tsunami and Lamb waves-induced ionospheric signatures generated by the 2022 Hunga Tonga volcanic eruption. Pure Appl Geophys. https://doi.org/10.1007/s00024-023-03271-5

Nakashima Y, Heki K, Takeo A, Cahyadi MN, Aditiya A, Yoshizawa K (2016) Atmospheric resonant oscillations by the 2014 eruption of the Kelud volcano, Indonesia, observed with the ionospheric total electron contents and seismic signals. Earth Planet Sci Lett 434:112–116. https://doi.org/10.1016/j.epsl.2015.11.029

NASA (2022) Tonga volcano plume reached the mesosphere. https://earthobservatory.nasa.gov/images/149474/tonga-volcano-plume-reached-the-mesosphere

NCEDC (2014) Northern California Earthquake Data Center. UC Berkeley Seismological Laboratory. Dataset (2014). https://doi.org/10.7932/NCEDC

Nickolaenko AP, Schekotov AY, Hayakawa M, Romero R, Izutsu J (2022) Electromagnetic manifestations of Tonga eruption in Schumann resonance band. J Atmos Sol Terr Phys 237:105897. https://doi.org/10.1016/j.jastp.2022.105897

Nishioka M, Tsugawa T, Kubota M, Ishii M (2013) Concentric waves and short-period oscillations observed in the ionosphere after the 2013 Moore EF5 tornado. Geophys Res Lett 40:5581–5586. https://doi.org/10.1002/2013GL057963

Nishitani N, Ruohoniemi JM, Lester M, Baker JBH, Koustov AV, Shepherd SG, Chisham G, Hori T, Thomas EG, Makarevich RA, Marchaudon A, Ponomarenko P, Wild JA, Milan SE, Bristow WA, Devlin J, Miller E, Greenwald RA, Ogawa T, Kikuchi T (2019) Review of the accomplishments of mid-latitude Super Dual Auroral Radar Network (SuperDARN) HF radars. Prog Earth Planet Sci 6:27. https://doi.org/10.1186/s40645-019-0270-5

Noll C (2010) The Crustal Dynamics Data Information System: A resource to support scientific analysis using space geodesy. Adv Space Res 45:1421–1440. https://doi.org/10.1016/j.asr.2010.01.018

Occhipinti G, Rolland L, Lognonné P, Watada S (2013) From Sumatra 2004 to Tohoku-Oki 2011: the systematic GPS detection of the ionospheric signature induced by tsunamigenic earthquakes. J Geophys Res 118:3626–3636. https://doi.org/10.1002/jgra.50322

Ogawa T, Kumagai H, Shinno K (1982) Ionospheric disturbances over Japan due to the 18 May 1980 eruption of Mount St. Helens. J Atmos Terr Phys 44:863–868. https://doi.org/10.1016/0021-9169(82)90039-3

Omira R, Ramalho RS, Kim J, González PJ, Kadri U, Miranda JM, Carrilho F, Baptista MA (2022) Global Tonga tsunami explained by a fast-moving atmospheric source. Nature 609:734–740. https://doi.org/10.1038/s41586-022-04926-4

Pacific Northwest Geodetic Array (PANGA), GPS/GNSS Network and Geodesy Laboratory: Central Washington University, other/seismic network. Int. Fed. of Digital Seismograph Networks (1996). https://doi.org/10.7914/SN/PW

Otsuka Y, Shiokawa K, Ogawa T, Wilkinson P (2002) Geomagnetic conjugate observations of equatorial airglow depletions. Geophys Res Lett 29:43. https://doi.org/10.1029/2002gl015347

Otsuka Y (2021) Medium-scale traveling ionospheric disturbances. In: Huang C, Lu G, Zhang Y, Paxton LJ (eds), Ionosphere dynamics and applications, pp 421–437. https://doi.org/10.1002/9781119815617.ch18

Perkins FW (1973) Spread F and ionospheric currents. J Geophys Res 78:218–226. https://doi.org/10.1029/JA078i001p00218

Pi X, Mannucci AJ, Lindqwister UJ, Ho CM (1997) Monitoring of global ionospheric irregularities using the Worldwide GPS Network. Geophys Res Lett 24:2283–2286. https://doi.org/10.1029/97GL02273

Piñón DA, Gómez DD, Smalley R, Cimbaro SR, Lauría EA, Bevis MG (2018) The history, state, and future of the Argentine continuous satellite monitoring network and its contributions to geodesy in Latin America, *Seismological Res*. Lett 89:475–482. https://doi.org/10.1785/0220170162

Pokhotelov OA, Parrot M, Pilipenko VA, Fedorov EN, Surkov VV, Gladyshev VA (1995) Response of the ionosphere to natural and man-made

acoustic sources. Ann Geophys 13:1197–1210. https://doi.org/10.1007/s00585-995-1197-2
Pradipta R, Carter BA, Currie JL, Choy S, Wilkinson P, Maher P, Marshall R (2023) On the propagation of traveling ionospheric disturbances from the Hunga Tonga–Hunga Ha'apai volcano eruption and their possible connection with tsunami waves. Geophys Res Lett 50:1. https://doi.org/10.1029/2022GL101925
Rajesh PK, Lin CCH, Lin JT, Lin CY, Liu JY, Matsuo T, Huang CY, Chou MY, Yue J, Nishioka N, Jin H, Choi JM, Chen SP, Chou M, Tsai HF (2022) Extreme poleward expanding super plasma bubbles over Asia-Pacific region triggered by Tonga volcano eruption during the recovery-phase of geomagnetic storm. Geophys Res Lett 49:e2022GL099798. https://doi.org/10.1029/2022GL099798
Rakesh V, Haridas S, Sivan C, Manoj MG, Abhilash S, Paul B, Unnikrishnan K, Mohanakumar K, Chandran RS (2022) Impact of the Hunga Tonga–Hunga Ha'apai volcanic eruption on the changes observed over the Indian near-equatorial ionosphere. Adv Space Res 70:2480–2493. https://doi.org/10.1016/j.asr.2022.07.004
Ravanelli M, Astafyeva E, Munaibari E, Rolland L, Mikesell TD (2023) Ocean-ionosphere disturbances due to the 15 January 2022 Hunga-Tonga Hunga-Ha'apai eruption. Geophys Res Lett 50:e2022GL101465. https://doi.org/10.1029/2022GL101465
RESIF, RESIF-RENAG French national geodetic network. RESIF-Reseau Sismologique et geodesique Francais (2017). https://doi.org/10.15778/resif.rg
Richmond AD (1979) Ionospheric wind dynamo theory: a review. J Geomag Geoelectr 31:287–310. https://doi.org/10.5636/jgg.31.287
Rolland LM, Occhipinti G, Lognonné P, Loevenbruck A (2010) Ionospheric gravity waves detected offshore Hawaii after tsunamis. Geophys Res Lett 37:L17101. https://doi.org/10.1029/2010GL044479
Saito S (2022) Ionospheric disturbances observed over Japan following the eruption of Hunga Tonga–Hunga Ha'apai on 15 January 2022. Earth Planets Space 74:57. https://doi.org/10.1186/s40623-022-01619-0
Schnepf NR, Minami T, Toh H, Nair MC (2022) Magnetic signatures of the 15 January 2022 Hunga Tonga–Hunga Ha'apai volcanic eruption. Geophys Res Lett 49:e2022GL098454. https://doi.org/10.1029/2022GL098454
Seo J, Walter T, Chiou T-Y, Enge P (2009) Characteristics of deep GPS signal fading due to ionospheric scintillation for aviation receiver design. Radio Sci 44:RS0A16. https://doi.org/10.1029/2008rs004077
Shestakov N, Orlyakovskiy A, Perevalova N, Titkov N, Chebrov D, Ohzono M, Takahashi H (2021) Investigation of ionospheric response to June 2009 Sarychev peak volcano eruption. Remote Sens 13:648. https://doi.org/10.3390/rs13040638
Shi JK, Wang GJ, Reinisch BW, Shang SP, Wang X, Zherebotsov G, Potekhin A (2011) Relationship between strong range spread F and ionospheric scintillations observed in Hainan from 2003 to 2007. J Geophys Res 116:A08306. https://doi.org/10.1029/2011JA016806
Shinagawa H, Iyemori T, Saito S, Maruyama T (2007) A numerical simulation of ionospheric and atmospheric variations associated with the Sumatra earthquake on December 26, 2004. Earth Planets Space 59:1015–1026. https://doi.org/10.1186/bf03352042
Shinbori A, Otsuka Y, Sori T, Nishioka M, Perwitasari S, Tsuda T, Nishitani N (2022) Electromagnetic conjugacy of ionospheric disturbances after the 2022 Hunga Tonga–Hunga Ha'apai volcanic eruption as seen in GNSS-TEC and SuperDARN Hokkaido pair of radars observations. Earth Planets Space 74:106. https://doi.org/10.1186/s40623-022-01665-8
Shinbori A, Sori T, Otsuka Y, Nishioka M, Perwitasari S, Tsuda T, Kumamoto A, Tsuchiya F, Matsuda S, Kasahara Y, Matsuoka A, Nakamura S, Miyoshi Y, Shinohara I (2023) Generation of equatorial plasma bubble after the 2022 Tonga volcanic eruption. Sci Rep. https://doi.org/10.1038/s41598-023-33603-3
Shults K, Astafyeva E, Adourian S (2016) Ionospheric detection and localization of volcano eruptions on the example of the April 2015 Calbuco events. J Geophys Res 121:10303–10315. https://doi.org/10.1002/2016JA023382
Sori T, Otsuka Y, Shinbori A, Nishioka M, Perwitasari S (2022) Geomagnetic conjugacy of plasma bubbles extending to mid-latitudes during a geomagnetic storm on March 1, 2013. Earth Planets Space 74:120. https://doi.org/10.1186/s40623-022-01682-7
Sun W, Kuriakose AK, Li G, Li Y, Zhao X, Hu L, Yang S, Xie H, Li Y, Ning B, Liu L (2022a) Unseasonal super ionospheric plasma bubble and scintillations seeded by the 2022 Tonga volcano eruption related perturbations. J Space Weather Space Clim 12:25. https://doi.org/10.1051/swsc/2022024
Sun Y-Y, Chen C-H, Lin C-Y (2022b) Detection of vertical changes in the ionospheric electron density structures by the radio occultation technique onboard the FORMOSAT-7/COSMIC2 mission over the eruption of the Tonga underwater volcano on 15 January 2022. Remote Sens 14:4266. https://doi.org/10.3390/rs14174266
Sun Y-Y, Chen C-H, Zhang P, Li S, Xu H-R, Yu T, Lin K, Mao Z, Zhang D, Lin C-Y, Liu J-Y (2022c) Explosive eruption of the Tonga underwater volcano modulates the ionospheric E-region current on 15 January 2022. Geophys Res Lett 49:e2022GL099621. https://doi.org/10.1029/2022GL099621
Tahira M (1995) Acoustic resonance of the atmospheric at 3.7 mHz. J Atmos Sci 52:2670–2674. https://doi.org/10.1175/1520-0469(1995)052%3c2670:arotaa%3e2.0.co;2
Takahashi H, Figueiredo CAOB, Barros D, Wrasse CM, Giongo GA, Honda RH, Vital LFR, Resende LCA, Nyassor PK, Ayorinde TT, Carmo CS, Padua MB, Otsuka Y (2023) Ionospheric disturbances over South America related to Tonga volcanic eruption. Earth Planets Space 75:92. https://doi.org/10.1186/s40623-023-01844-1
Tang L (2023) Ionospheric disturbances of the January 15, 2022, Tonga volcanic eruption observed using the GNSS network in New Zealand. GPS Sol 27:53. https://doi.org/10.1007/s10291-023-01395-8
Tanioka Y, Yamanaka Y, Nakagaki T (2022) Characteristics of the deep sea tsunami excited offshore Japan due to the air wave from the 2022 Tonga eruption. Earth Planets Space 74:61. https://doi.org/10.1186/s40623-022-01614-5
Themens DR, Watson C, Žagar N, Vasylkevych S, Elvidge S, McCaffrey A, Prikryl P, Reid B, Wood A, Jayachandran PT (2022) Global propagation of ionospheric disturbances associated with the 2022 Tonga volcanic eruption. Geophys Res Lett 49:e2022GL098158. https://doi.org/10.1029/2022GL098158
Vadas SL, Becker E, Figueiredo C, Bossert K, Harding BJ, Gasque LC (2023a) Primary and secondary gravity waves and large-scale wind changes generated by the Tonga volcanic eruption on 15 January 2022: modeling and comparison with ICON-MIGHTI winds. J Geophys Res 128:e2022JA031138. https://doi.org/10.1029/2022JA031138
Vadas SL, Figueiredo C, Becker E, Huba JD, Themens DR, Hindley NP, Mrak S, Galkin I, Bossert K (2023b) Traveling ionospheric disturbances induced by the secondary gravity waves from the Tonga eruption on 15 January 2022: modeling with MESORAC-HIAMCMSAMI3 and comparison with GPS/TEC and ionosonde data. J Geophys Res 128:e2023JA031408. https://doi.org/10.1029/2023JA031408
Verhulst TGW, Altadill D, Barta V, Belehaki A, Buresova D, Cesaroni C, Galkin I, Guerra M, Ippolito A, Herekakis T, Kouba D, Mielich J, Segarra A, Spogli L, Tsagouri I (2022) Multi-instrument detection in Europe of ionospheric disturbances caused by the 15 January 2022 eruption of the Hunga volcano. J Space Weather Space Clim 12:35. https://doi.org/10.1051/swsc/2022032
Wang H, Xia H, Zhang K (2022) Variations in the equatorial ionospheric F region current during the 2022 Tonga volcanic eruption. Remote Sens 14:6241. https://doi.org/10.3390/rs14246241
Watanabe S, Hamilton K, Sakazaki T, Nakano M (2022) First detection of the Pekeris internal global atmospheric resonance: evidence from the 2022 Tonga eruption and from global reanalysis data. J Atmos Sci 79:3027–3043. https://doi.org/10.1175/JAS-D-22-0078.1
Wright CJ, Hindley NP, Alexander MJ, Barlow M, Hoffmann L, Mitchell CN, Prata F, Bouillon M, Carstens J, Clerbaux C, Osprey SM, Powell N, Randall CE, Yue J (2022) Surface-to-space atmospheric waves from Hunga Tonga–Hunga Ha'apai eruption. Nature 609:741–746. https://doi.org/10.1038/s41586-022-05012-5
Yamazaki Y, Maute A (2017) Sq and EEJ—a review on the daily variation of the geomagnetic field caused by ionospheric dynamo currents. Space Sci Rev 206:299–405. https://doi.org/10.1007/s11214-016-0282-z
Yamazaki Y, Richmond AD, Maute A, Liu H-L, Pedatella N, Sassi F (2014) On the day-to-day variation of the equatorial electrojet during quiet periods. J Geophys Res 119:6966–6980. https://doi.org/10.1002/2014JA020243
Yamazaki Y, Harding BJ, Stolle C, Matzka J (2021) Neutral wind profiles during periods of eastward and westward equatorial electrojet. Geophys Res Lett 48:1–10. https://doi.org/10.1029/2021GL093567

Yamazaki Y, Soares G, Matzka J (2022) Geomagnetic detection of the atmospheric acoustic resonance at 3.8 mHz during the Hunga Tonga eruption event on 15 January 2022. J Geophys Res 127:e2022JA030540. https://doi.org/10.1029/2022JA030540

Zettergren M, Snively J (2019) Latitude and longitude dependence of ionospheric TEC and magnetic perturbations from infrasonic–acoustic waves generated by strong seismic events. Geophys Res Lett 46:1132–1140. https://doi.org/10.1029/2018gl081569

Zhang J, Xu J, Wang W, Wang G, Ruohoniemi JM, Shinbori A, Nishitani N, Wang C, Deng X, Lan A, Yan J (2022a) Oscillations of the ionosphere caused by the 2022 Tonga volcanic eruption observed with SuperDARN radars. Geophys Res Lett 49:e2022GL100555. https://doi.org/10.1029/2022GL100555

Zhang K, Wang H, Zhong Y, Xia H, Qian C (2022b) The temporal evolution of F-region equatorial ionization anomaly owing to the 2022 Tonga volcanic eruption. Remote Sens 14:5714. https://doi.org/10.3390/rs14225714

Zhao W, Sun C, Guo Z (2022) Reawaking of Tonga volcano. Innov 3:100218. https://doi.org/10.1016/j.xinn.2022.100218

Zhou M, Gao H, Yu D, Guo J, Zhu L, Yang L, Pan S (2022) Analysis of the anomalous environmental response to the 2022 Tonga volcanic eruption based on GNSS. Remote Sens 14:4847. https://doi.org/10.3390/rs14194847

Publisher's Note